

CASL: Concept-Aligned Sparse Latents for Interpreting Diffusion Models

Zhenghao He, Guangzhi Xiong, Boyang Wang, Sanchit Sinha, Aidong Zhang
 University of Virginia, USA
 {zhenghao, guangzhi, usy5km, sanchit, aidong}@virginia.edu

Abstract

*Internal activations of diffusion models encode rich semantic information, but interpreting such representations remains challenging. While Sparse Autoencoders (SAEs) have shown promise in disentangling latent representations, existing SAE-based methods for diffusion model understanding rely on unsupervised approaches that fail to align sparse features with human-understandable concepts. This limits their ability to provide reliable semantic control over generated images. We introduce **CASL** (Concept-Aligned Sparse Latents), a supervised framework that aligns sparse latent dimensions of diffusion models with semantic concepts. CASL first trains an SAE on frozen U-Net activations to obtain disentangled latent representations, and then learns a lightweight linear mapping that associates each concept with a small set of relevant latent dimensions. To validate the semantic meaning of these aligned directions, we propose **CASL-Steer**, a controlled latent intervention that shifts activations along the learned concept axis. Unlike editing methods, CASL-Steer is used solely as a causal probe to reveal how concept-aligned latents influence generated content. We further introduce the **Editing Precision Ratio (EPR)**, a metric that jointly measures concept specificity and the preservation of unrelated attributes. Experiments show that our method achieves superior editing precision and interpretability compared to existing approaches. To the best of our knowledge, this is the first work to achieve supervised alignment between latent representations and semantic concepts in diffusion models.*

1. Introduction

Diffusion models have achieved remarkable success in image generation. Recent studies [13, 19, 26, 30] have revealed that internal activations of diffusion models already exhibit rich semantic properties, with high-level concepts implicitly represented within their feature spaces. In the field of natural language processing, Sparse Autoencoders (SAEs) have proven effective in disentangling latent semantics from internal activations [5]. Recent works have begun

to adapt this approach to diffusion models, aiming to extract interpretable features from hidden activations during generation [11, 12, 25, 28]. These efforts show promises in revealing meaningful structures within the high-dimensional hidden states of diffusion models.

However, extending sparse interpretability to vision diffusion models remains challenging. Existing attempts rely on unsupervised SAEs that attribute semantics to each latent unit by identifying the input that maximally activates it. While this heuristic is effective in NLP, where discrete tokens naturally serve as semantic anchors, it breaks down in vision settings. Image representations are continuous, spatially distributed, and heavily entangled, meaning that high activations often reflect a mixture of correlated attributes rather than a single interpretable concept. For instance, the notion of “smiling” co-occurs with changes in the mouth, cheeks, eyes, and global facial geometry, making it unclear which latent unit should be associated with the concept itself. As a result, current vision SAEs struggle to produce consistent, concept-specific latent directions, limiting their ability to support meaningful interpretation or controlled intervention.

To overcome these limitations, we introduce CASL, a framework that learns concept-aligned sparse latents in diffusion models. CASL first trains a Sparse Autoencoder on frozen U-Net activations to obtain a disentangled latent space. Then, instead of relying on unsupervised heuristics, we incorporate weak supervision to learn a lightweight linear mapping that associates each concept with its most relevant sparse dimensions. This yields a set of concept-aligned latent directions that are suitable for semantic interpretation. To verify their semantic effect, we further apply CASL-Steer, a controlled latent intervention that perturbs activations along the aligned direction to evaluate how each concept influences the model’s generative behavior.

Our main contributions are summarized as follows:

- We introduce **CASL**, a supervised framework that learns concept-aligned sparse latents in diffusion models. To our knowledge, this is the first method to explicitly align SAE latent dimensions in diffusion models with human-defined semantic concepts.

- We propose **CASL-Steer**, a controlled latent intervention used to validate the semantic effects of the aligned latent directions. CASL-Steer serves as a causal probe for interpretability rather than an image editing method.
- We design the **Editing Precision Ratio (EPR)**, a quantitative metric that jointly measures semantic specificity and the preservation of unrelated attributes, enabling systematic evaluation of concept alignment in sparse latent spaces.

2. Related Work

Semantic Editing in Diffusion Models. Diffusion models have demonstrated impressive capabilities in semantic image editing by conditioning the generation process on user-defined signals. Early methods such as SDEdit [20] apply noise to input images and guide the denoising trajectory via external conditioning, achieving structure-preserving edits. Prompt-based approaches like DiffusionCLIP [18], InstructPix2Pix [2], and Imagic [16] steer generation using language or visual instructions, typically requiring fine-tuning of the diffusion model. In contrast, methods such as Prompt-to-Prompt [8], Asyrrp [19], and Concept Sliders [7] explore direct intervention into internal representations of a frozen U-Net, enabling localized edits without retraining. Among them, Asyrrp proposes lightweight, learnable residual modules inserted into intermediate layers to control semantic attributes. However, despite their effectiveness, these methods still operate as black boxes and provide little insight into how internal activations correspond to human-interpretable concepts—a gap our work seeks to address.

Sparse and Interpretable Representations. Sparse Autoencoders (SAEs) have shown promise in learning human-interpretable representations by enforcing sparsity on latent activations. In natural language processing (NLP), SAEs trained on frozen transformer features have been shown to produce sparse latent dimensions that align with interpretable linguistic features, such as sentiment, negation, or syntactic structures [1, 5]. This has inspired efforts to adapt SAE-based analysis to the vision domain, including generative models.

Recent studies have begun to explore SAE-based interpretation within diffusion models. Surkov et al. [25] and Ijishakin et al. [12] both train SAEs on internal residual or bottleneck activations and demonstrate that manipulating individual latent units can causally affect generation. However, in the absence of semantic supervision, the learned features must be interpreted post-hoc and lack consistent alignment with human concepts. Huang et al. [11] extend this paradigm to diffusion transformers, proposing a temporal-aware SAE architecture that captures denoising dynamics across timesteps. While their method improves

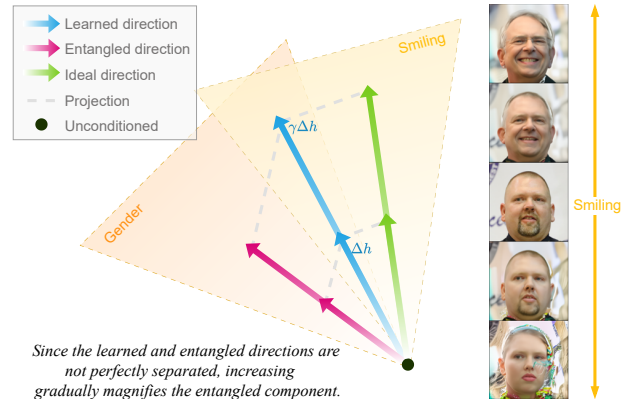


Figure 1. Demonstration of semantic directions in the activation space. Left: Geometric illustration of ideal, entangled, and learned semantic directions in the activation space. Right: scaling the Asyrrp direction $\Delta h^{(\text{smile})}$ from $\gamma = -2$ to $\gamma = 2$ increases smiling intensity, but also introduces entangled changes in identity, hairstyle, and gender.

feature disentanglement and supports classification, the latent space remains entangled with temporal and visual factors, and offers limited control over semantic content. Kim et al. [17] adopt a more diagnostic perspective, using k-sparse autoencoders to analyze semantic granularity across layers and timesteps in various architectures. Although their analysis reveals monosemantic trends and enables transfer learning, it does not target controllable editing.

Our approach introduces explicit concept-level supervision to directly align sparse latent units with human-interpretable concepts. This supervision ensures that specific latent features consistently reflect the presence or absence of target semantic attributes, enabling faithful and interpretable control over diffusion-based generation.

3. Problem Formulation

U-Net Activations (h -space). Following [12, 19, 28, 30], we similarly denote the intermediate activation (h -space) of a diffusion model’s U-Net at a specific layer at $h \in \mathbb{R}^{C \times H \times W}$, where C , H , and W denote the number of channels, height, and width, respectively. Prior works [19, 30] have shown that h encodes rich semantic information and can be directly edited to control high-level concepts.

DDIM Sampling. We adopt the DDIM sampling schedule [23] for deterministic denoising, which enables applying controlled interventions in h -space without introducing stochastic variation. Kwon et al. [19] introduces a learnable shift Δh_t in the U-Net bottleneck, modifying only the P_t term of the DDIM update:

$$x_{t-1} = \sqrt{\alpha_{t-1}} P_t(\epsilon_\theta(x_t | \Delta h_t)) + D_t(\epsilon_\theta(x_t)). \quad (1)$$

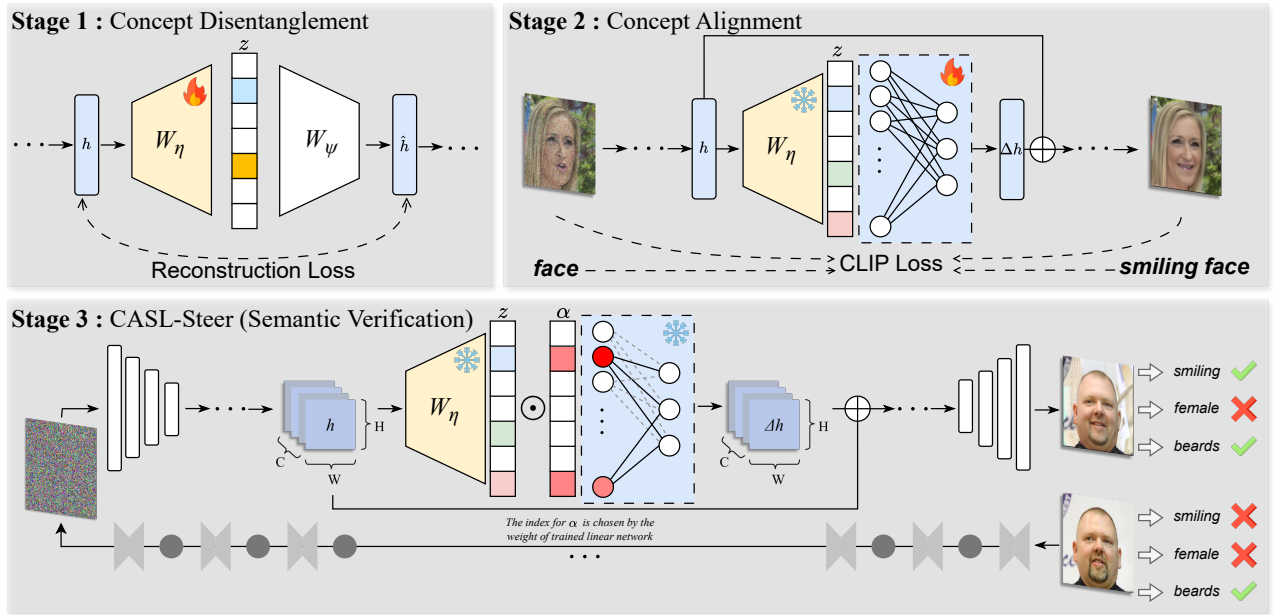


Figure 2. Overview of our proposed CASL framework. **Stage 1 (Concept Disentanglement):** A Sparse Autoencoder is trained on U-Net activations to obtain a structured sparse latent representation. **Stage 2 (Concept Alignment):** A lightweight linear mapping aligns selected latent dimensions with human-defined semantic concepts, producing concept-aligned directions. **Stage 3 (CASL-Steer):** A controlled latent intervention is applied along the aligned direction to *verify* its semantic effect, serving as a probing mechanism.

This asymmetric activation-space injection enables controlled semantic manipulation without altering the overall generative trajectory.

Structured Latent Hypothesis. Empirical activation-space editing often exhibits entanglement: increasing the edit scale γ_c strengthens the target attribute but simultaneously alters identity, background, or lighting. We argue that this arises because the learned direction $\Delta h^{(c)}$ is not a pure concept vector, but instead a mixture of multiple semantic components. Small edits suppress these mixed factors, while larger edits amplify them (see Fig. 1).

To explain this behavior, we hypothesize that each concept direction $\Delta h^{(c)}$ admits a *sparse expansion* over a shared set of latent semantic bases. Specifically, there exist basis elements $\{b_i\}_{i=1}^K \subset \mathbb{R}^{C \times H \times W}$ such that

$$\Delta h^{(c)} = \sum_{i=1}^K \beta_i^{(c)} b_i, \quad \|\beta^{(c)}\|_0 \ll K. \quad (2)$$

Here, $\{b_i\}$ represent underlying semantic directions, and $\beta^{(c)}$ encodes the concept's coordinates in this basis. Our goal is to learn this structured latent space and align selected basis directions with human-defined concepts.

4. Method

Our framework consists of three main stages: (1) We train a sparse autoencoder (SAE) to encode U-Net activations into

a structured and interpretable latent space (Sec. 4.1). (2) We align selected latent dimensions with human-defined concepts by learning a lightweight linear mapping under semantic supervision (Sec. 4.2). (3) We verify the semantic effect of the aligned directions through a controlled latent intervention in activation space (Sec. 4.3). In addition, we propose a metric to measure the effectiveness of aligning the latent representation with the semantic concepts (Sec. 4.4). Fig. 2 illustrates the main components of our framework and their relationships.

4.1. Concept Disentanglement (Stage 1)

Given an input activation $h \in \mathbb{R}^{C \times H \times W}$ from a diffusion model, we reshape h into $N = H \times W$ tokens of dimension C , i.e., $h_{\text{seq}} \in \mathbb{R}^{N \times C}$. Following [11, 25], each spatial location is treated as a token, and SAE maps h_{seq} to sparse latent $z \in \mathbb{R}^{N \times K}$, where $K \gg C$.

The encoding and decoding processes are defined as:

$$z^{(t)} = \phi \left(W_\eta(h^{(t)} + e(t) - b_{\text{pre}}) + b_\eta \right) \quad (3)$$

$$\hat{h}^{(t)} = W_\psi z^{(t)} + b_{\text{pre}} \quad (4)$$

where $h^{(t)} \in \mathbb{R}^{N \times C}$ is the U-Net activation at timestep t , and $z^{(t)} \in \mathbb{R}^{N \times K}$ is its sparse latent representation. The term $e(t) \in \mathbb{R}^C$ is a learnable timestep embedding added to $h^{(t)}$ before encoding. The encoder is a linear transformation $W_\eta \in \mathbb{R}^{K \times C}$ without bias, followed by a latent bias

$b_\eta \in \mathbb{R}^K$ and an element-wise activation function $\phi(\cdot)$. The decoder is also linear, $W_\psi \in \mathbb{R}^{C \times K}$, without bias. A learnable pre-bias vector $b_{\text{pre}} \in \mathbb{R}^C$ is subtracted from the input before encoding and added back after decoding to restore the original activation space.

The overall objective for training the SAE is:

$$\mathcal{L}_{\text{SAE}} = \underbrace{\|h - \hat{h}\|_2^2}_{\text{Reconstruction Loss}} + \underbrace{\lambda_{\text{sparse}} \|z\|_1}_{\text{Sparsity}} \quad (5)$$

where λ_{sparse} controls the strength of sparsity regularization.

4.2. Concept Alignment (Stage 2)

After training the SAE, we freeze its encoder W_η and perform inversion to obtain the disentangled latent representation $z = W_\eta(h)$ for each input activation h .

To align specific latent dimensions z_i with human-defined concepts (e.g., *smiling*), we introduce a lightweight linear mapping without any activation function that predicts the concept editing direction in the activation space:

$$\Delta h = W_\Delta z + b_\Delta \quad (6)$$

where $W_\Delta \in \mathbb{R}^{C \times K}$ and $b_\Delta \in \mathbb{R}^C$ are learnable parameters.

The edited activation is computed as $h' = h + \Delta h$, which is injected into the U-Net to compute the modified noise prediction. We then use this modified output in the DDIM inversion formula to obtain the edited image:

$$\hat{x}_0^{\text{edit}} = \frac{1}{\sqrt{\alpha_t}} (x_t - \sqrt{1 - \alpha_t} \cdot \varepsilon_\theta(x_t | h + \Delta h)) \quad (7)$$

To ensure that Δh effectively induces the desired concept change (e.g., adding a smile), we follow [19] and combine the DiffusionCLIP loss [18] with an L1 regularization term:

$$\begin{aligned} \mathcal{L} = & \lambda_{\text{CLIP}} \mathcal{L}_{\text{DiffusionCLIP}}(\hat{x}_0^{\text{edit}}, y^{\text{ref}}; x_0^{\text{origin}}, y^{\text{origin}}) \\ & + \lambda_{\text{recon}} \|\hat{x}_0^{\text{edit}} - x_0^{\text{origin}}\|_1 \end{aligned} \quad (8)$$

where \hat{x}_0^{edit} denotes the generated image after applying the edited latent representation, and x_0^{origin} is the input image without editing. y^{ref} and y^{origin} are the corresponding CLIP text embeddings of the target and original semantic descriptions, respectively.

Through this process, the model learns to associate certain latent dimensions in z with explicit semantic concepts, enabling controllable and interpretable concept editing.

4.3. CASL-Steer: Semantic Verification (Stage 3)

Building on the concept alignment in Section 4.2, We aim to verify whether the learned sparse latent directions correspond to distinct, human-interpretable semantic concepts

in the activation space, rather than focusing on image editing. To this end, we construct explicit mathematical formulations that enable principled and quantitative evaluation of concept alignment and disentanglement.

Firstly, we construct a sparse latent coordinate vector $\alpha \in \mathbb{R}^K$, where each entry specifies the traversal strength along a particular semantic direction. For a given concept c , we first select the top- k latent dimensions as:

$$\mathcal{I}_c = \text{TopK}_k \left(\left| W_\Delta^{(c)} \right| \right) \quad (9)$$

where $\left| W_\Delta^{(c)} \right|$ denotes the element-wise absolute value of the learned editing weights for concept c .

We then define the editing coordinate as

$$\alpha_i = \begin{cases} \alpha, & \text{if } i \in \mathcal{I}_c \\ 0, & \text{otherwise} \end{cases} \quad (10)$$

where α controls the editing intensity. This construction ensures that editing is only applied along concept-specific, disentangled semantic directions.

Given a disentangled semantic basis z for the current activation (obtained from the SAE encoder), the concept-wise editing direction in activation space is computed as:

$$\Delta h_c = W_\Delta \left(\underbrace{\alpha}_{\substack{\text{coordinate in} \\ \text{semantic basis}}} \odot \underbrace{z}_{\substack{\text{sparse} \\ \text{semantic basis}}} \right) \quad (11)$$

where \odot denotes element-wise multiplication, z represents the semantic basis vectors in the activation space, and α specifies the editing coordinate in this basis. The resulting activation shift Δh_c is then added to the original activation, and the edited image \hat{x}_0 is obtained following the same DDIM inversion process as described in Section 4.2.

4.4. Editing Precision Ratio (EPR)

A desirable causal probing metric should induce significant changes in the target attribute while minimizing unintended modifications to other (non-target) attributes. However, existing evaluation metrics do not jointly measure the degree of the *editing effectiveness* on the target attribute and the side effects on the non-target attributes. To address this, we propose a metric called *Editing Precision Ratio* (EPR), which provides a unified and interpretable metric.

Given N pairs of original and edited images $\{x_i, x'_i\}_{i=1}^N$, let $f_{\text{target}}(\cdot)$ denote the classifier score for the target attribute, and $f_j(\cdot)$ denote the classification score for the j -th non-target attribute (for $j = 1, \dots, L$).

Average Target Attribute Change (Editing Effectiveness). This term captures how much the editing on the target attribute shifts the score of the target attribute:

$$\Delta_{\text{target}} = \frac{1}{N} \sum_{i=1}^N |f_{\text{target}}(x'_i) - f_{\text{target}}(x_i)| \quad (12)$$

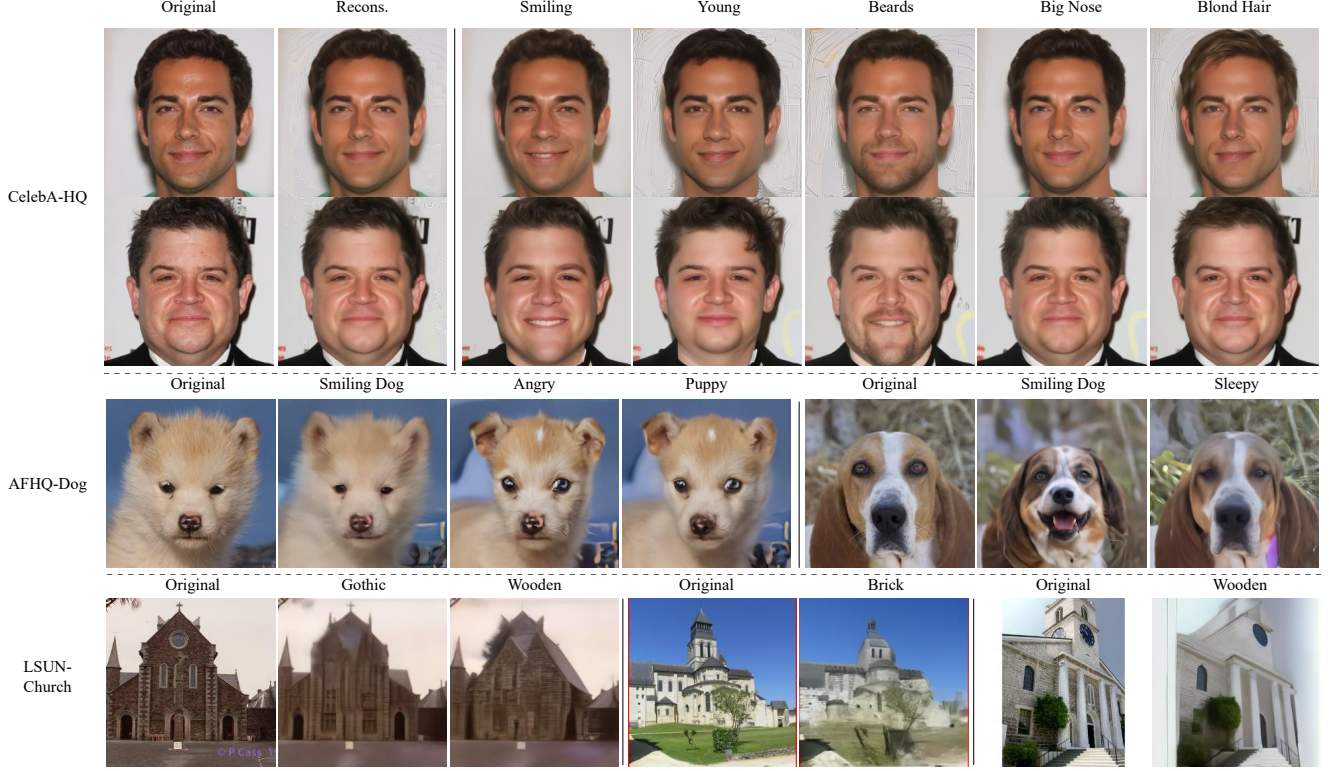


Figure 3. Attribute editing results of concept-aligned editing. Our method enables concept-aligned editing across diverse attributes and domains. Each column shows a specific attribute (*Smiling*, *Young*, *Puppy*, etc.) with consistent edits across different identities. Results are obtained by traversing sparse latent dimensions learned through supervised alignment.

Average Non-Target Attribute Change (Side Effects).

This term reflects the average change across all unrelated attributes, measuring how much collateral change the edit induces on all the non-target attributes:

$$\Delta_{\text{non_target}} = \frac{1}{L} \sum_{j=1}^L \left(\frac{1}{N} \sum_{i=1}^N |f_j(x'_i) - f_j(x_i)| \right) \quad (13)$$

Editing Precision Ratio. The final score is defined as the ratio between the average target attribute change and the average non-target attribute change:

$$\text{EPR} = \frac{\Delta_{\text{target}}}{\Delta_{\text{non_target}} + \epsilon} \quad (14)$$

where ϵ is a small constant added for numerical stability.

A higher EPR indicates that the editing method achieves greater changes in the target attribute with less unintended change to non-target attributes, thus providing a quantitative measure of both editing effectiveness on the target attribute and side effects on the non target attributes. In practice, f_j denotes the classifier logits rather than probabilities, as logits preserve relative semantic strength without saturation. We set $\epsilon = 10^{-8}$ for numerical stability.

5. Experiments

5.1. Implementation Details

We evaluate CASL on multiple datasets, including FFHQ [15], CelebA-HQ [14], LSUN-Church [27] and AFHQ [4]. For each dataset, we adopt the corresponding diffusion backbone: DDPM++ [24] for FFHQ and CelebA-HQ, DDPM [10] for LSUN and iDDPM [22] for AFHQ. All diffusion backbones are official pretrained checkpoints and remain frozen. We uniformly sample 50 timesteps between $t = 999$ and $t = 500$ and extract the associated U-Net activations. The Sparse Autoencoder is trained on bottleneck activations, after which we learn a lightweight linear mapping for each concept using 1,000 real images. Full training configurations and runtime statistics are provided in the Appendix. All experiments are run on 1 NVIDIA RTX A100 GPU (80GB memory). More implementation details can be found in Appendix.

5.2. Visual Validation of Concept Alignment

Figure 3 provides a qualitative validation of whether the concept-aligned latent directions learned by CASL correspond to the intended semantics and whether the resulting interventions remain localized and disentangled.

Concept	Metric	Recon.	Editing Methods					Explainable CASL-Steer
			Boundary [30]	Asymp [19]	Slider [7]	MasaCtrl [3]	SwiftEdit [21]	
Smiling	EPR (\uparrow)	0.679 \pm 0.289	1.231 \pm 0.976	3.199 \pm 2.182	0.949 \pm 0.479	1.685 \pm 1.375	3.359 \pm 2.064	4.465 \pm 2.319
	CLIP-Score [9] (\uparrow)	0.126 \pm 0.014	0.166 \pm 0.012	0.192 \pm 0.014	0.178 \pm 0.010	0.204 \pm 0.013	0.171 \pm 0.015	0.192 \pm 0.012
	LPIPS [29] (\downarrow)	0.169 \pm 0.057	0.251 \pm 0.049	0.358 \pm 0.086	0.487 \pm 0.076	0.678 \pm 0.246	0.251 \pm 0.052	0.243 \pm 0.085
	ArcFace [6] (\uparrow)	0.943 \pm 0.037	0.564 \pm 0.144	0.238 \pm 0.144	0.540 \pm 0.061	0.193 \pm 0.184	0.358 \pm 0.123	0.566 \pm 0.210
Big Nose	EPR (\uparrow)	0.207 \pm 0.280	0.882 \pm 0.539	0.938 \pm 0.608	1.035 \pm 0.775	0.793 \pm 0.600	0.867 \pm 0.627	1.060 \pm 0.608
	CLIP-Score (\uparrow)	0.140 \pm 0.019	0.148 \pm 0.014	0.173 \pm 0.017	0.168 \pm 0.012	0.200 \pm 0.029	0.157 \pm 0.014	0.159 \pm 0.012
	LPIPS (\downarrow)	0.169 \pm 0.057	0.270 \pm 0.055	0.275 \pm 0.082	0.546 \pm 0.078	0.699 \pm 0.231	0.208 \pm 0.048	0.191 \pm 0.050
	ArcFace (\uparrow)	0.943 \pm 0.037	0.545 \pm 0.112	0.463 \pm 0.182	0.487 \pm 0.084	0.200 \pm 0.191	0.412 \pm 0.121	0.761 \pm 0.059
Young	EPR (\uparrow)	0.773 \pm 0.619	1.411 \pm 0.909	1.685 \pm 1.220	0.937 \pm 0.770	1.427 \pm 0.709	1.536 \pm 0.989	1.817 \pm 1.117
	CLIP-Score (\uparrow)	0.113 \pm 0.013	0.180 \pm 0.014	0.211 \pm 0.014	0.184 \pm 0.013	0.204 \pm 0.017	0.184 \pm 0.013	0.206 \pm 0.013
	LPIPS (\downarrow)	0.169 \pm 0.057	0.258 \pm 0.065	0.343 \pm 0.082	0.567 \pm 0.082	0.678 \pm 0.246	0.309 \pm 0.052	0.305 \pm 0.082
	ArcFace (\uparrow)	0.943 \pm 0.037	0.546 \pm 0.139	0.306 \pm 0.139	0.646 \pm 0.095	0.266 \pm 0.191	0.357 \pm 0.128	0.387 \pm 0.142
Beards	EPR (\uparrow)	0.763 \pm 0.669	1.165 \pm 0.974	1.739 \pm 1.268	0.919 \pm 0.383	2.059 \pm 1.541	1.255 \pm 0.884	2.161 \pm 1.080
	CLIP-Score (\uparrow)	0.112 \pm 0.033	0.134 \pm 0.038	0.206 \pm 0.047	0.132 \pm 0.032	0.204 \pm 0.022	0.141 \pm 0.031	0.211 \pm 0.043
	LPIPS (\downarrow)	0.169 \pm 0.057	0.274 \pm 0.054	0.353 \pm 0.090	0.490 \pm 0.073	0.741 \pm 0.216	0.257 \pm 0.053	0.233 \pm 0.071
	ArcFace (\uparrow)	0.943 \pm 0.037	0.550 \pm 0.116	0.294 \pm 0.164	0.542 \pm 0.058	0.171 \pm 0.191	0.422 \pm 0.136	0.562 \pm 0.260
Blond Hair	EPR (\uparrow)	0.110 \pm 0.032	0.876 \pm 0.794	1.173 \pm 1.002	0.760 \pm 0.548	1.173 \pm 0.678	1.302 \pm 1.014	1.386 \pm 1.213
	CLIP-Score (\uparrow)	0.143 \pm 0.029	0.153 \pm 0.030	0.186 \pm 0.039	0.143 \pm 0.027	0.185 \pm 0.021	0.154 \pm 0.033	0.170 \pm 0.036
	LPIPS (\downarrow)	0.169 \pm 0.057	0.262 \pm 0.052	0.303 \pm 0.082	0.491 \pm 0.076	0.713 \pm 0.208	0.227 \pm 0.103	0.221 \pm 0.072
	ArcFace (\uparrow)	0.943 \pm 0.037	0.547 \pm 0.117	0.409 \pm 0.210	0.544 \pm 0.053	0.169 \pm 0.128	0.387 \pm 0.141	0.686 \pm 0.155

Table 1. Our explainable editing framework achieves superior attribute manipulation performance without degrading perceptual quality or identity consistency. We evaluate five facial attributes using EPR, CLIP-Score, LPIPS, and ArcFace across all methods. We highlight the best value in green with bold text and the second best value in blue .

Across CelebA-HQ, the aligned directions consistently induce the intended semantic change (e.g., *Smiling*, *Young*, *Beards*) while leaving identity, background, and pose largely unchanged. This indicates that the learned latent units capture concept-specific information rather than mixed or correlated factors.

On AFHQ-Dog and LSUN-Church, CASL-Steer exhibits a similar behavior: concept directions such as *Smiling Dog*, *Puppy*, *Gothic*, and *Wooden* produce coherent semantic shifts while preserving viewpoint, geometry, and low-level appearance. The stability of the edits across categories suggests that the aligned latent space carries transferable and structurally meaningful concept directions.

Overall, these observations validate that the aligned latent dimensions learned by CASL correspond to stable and interpretable semantic factors. Manipulating a single dimension produces a targeted shift along the intended concept with little influence on unrelated factors, indicating that CASL successfully separates concept-relevant information from background variation.

Additional examples are provided in the Appendix to further confirm that CASL captures clean and interpretable concept directions with minimal collateral change.

5.3. Quantitative Evaluation

Our goal is not to introduce a new editing algorithm, but to use semantic editing as a causal probe for verifying whether a supervised sparse latent direction truly corresponds to a human-defined concept. We therefore compare CASL-Steer against representative attribute-editing methods that operate through activation-space or directional manipulations, including BoundaryDiffusion [30], Asymp [19], Concept Slider [7], MasaCtrl [3], and SwiftEdit [21]. We report four metrics commonly used in facial attribute editing: CLIP-Score [9] for semantic alignment, LPIPS [29] for perceptual distortion, ArcFace similarity [6] for identity preservation, and our proposed EPR (Sec. 4.4) for measuring the trade-off between attribute strength and unintended changes.

Table 1 shows results on CelebA-HQ. For each attribute, we randomly sample 32 images from the test split and use only the top-1 aligned latent dimension from CASL. CASL-Steer injects the concept-aligned shift once during the DDIM sampling process, while all baseline methods follow their standard configurations. Additional results with more datasets and a broader range of concepts are provided in the Appendix.

Reconstruction Baseline. The “Recon.” baseline corresponds to passing the input image through the inversion/reconstruction pipeline without applying any concept direction. This baseline is *not* an identity mapping, as the DDIM inversion and U-Net bottleneck reconstruction introduce small but non-negligible deviations in h -space. Consequently, its EPR is non-zero. We include this baseline to contextualize how much attribute drift arises purely from the inversion process, separating it from concept-specific changes.

Editing Strength. Across all concepts, CASL-Steer achieves competitive or superior CLIP-Score compared to LoRA-based (Slider) and training-free (SwiftEdit) methods, despite not updating the diffusion model. This indicates that the concept-aligned sparse directions learned by CASL capture the target semantic effect reliably.

Unintended Changes. CASL-Steer exhibits markedly fewer unintended modifications, as reflected by substantially lower LPIPS and higher ArcFace similarity. This suggests that aligning sparse latent dimensions with human-defined concepts leads to more localized and disentangled effects, while black-box methods often introduce changes correlated with the target concept (e.g., identity shift for “smiling” or background leakage for “blond hair”).

Editing Precision (EPR). Our EPR metric jointly measures target-attribute strength and collateral distortion. CASL-Steer consistently achieves the highest EPR across all concepts, demonstrating that concept-aligned sparse latents enable more precise and cleaner semantic shifts. Notably, CASL-Steer achieves the largest improvements on attributes that are typically entangled with other facial factors (e.g., *young* often correlates with smooth skin, and *blond hair* correlates with specific color tones). This suggests that supervised concept alignment helps separate the target attribute from its co-occurring correlated features.

5.4. Evaluation of Sparse Feature Representations

We evaluate the reconstruction quality and sparsity of the sparse autoencoder (SAE) representations as indicators of interpretability. Reconstruction is measured by mean squared error (MSE) and cosine similarity between original and reconstructed activations. Sparsity is quantified by the dimension activation ratio (DAR):

$$\text{DAR}(z) = \frac{1}{K} \sum_{j=1}^K \mathbb{I} \left[\frac{1}{N} \sum_{i=1}^N z_{ij} > \tau \right] \quad (15)$$

where $z \in \mathbb{R}^{N \times K}$ is the latent activation matrix and τ is a fixed threshold. Here, K is determined by a predefined expansion ratio γ_{sae} multiplied by the input channel dimension C . Lower DAR indicates a sparser representation.

Params	MSE($\times 10^{-2}$) ↓	Cosine Sim. ↑	DAR ($\times 10^{-2}$) ↓
$\gamma_{\text{sae}} = 16$	9.27	0.965	6.32
$\gamma_{\text{sae}} = 32$	5.39	0.980	3.54
$\gamma_{\text{sae}} = 64$	3.19	0.988	1.87
$\gamma_{\text{sae}} = 128$	1.91	0.993	1.08
$\gamma_{\text{sae}} = 256$	0.94	0.996	0.70
$\gamma_{\text{sae}} = 512$	0.56	0.998	0.39

Table 2. Reconstruction quality and sparsity of the SAE across different expansion ratios γ_{sae} . MSE and DAR values are scaled by 10^{-2} for readability.

Table 5 reports SAE performance across different expansion ratios γ_{sae} on CelebA-HQ, with input activations $h^{(t)}$ sampled uniformly from 50 timesteps between $t = 999$ and $t = 500$ during the DDIM inversion process. All configurations achieve low reconstruction error while maintaining strong sparsity, demonstrating the effectiveness of our design. Implementation details of the SAE and additional experiments with varying λ_{sparse} values are provided in the Appendix. We adopt $\gamma_{\text{sae}} = 128$ and sparsity weight $\lambda_{\text{sparse}} = 32$ as default for balancing performance and efficiency.

5.5. Concept Alignment Evaluation

To evaluate whether CASL successfully aligns specific latent dimensions z_i to human-defined concepts, we perform a classification-based probing experiment. For each concept c , we select the top- k latent units according to \mathcal{I}_c (Eq. 9) and train a linear SVM classifier using these k -dimensional features.

As is shown in Table 3, the experiments are conducted under the hyperparameter setting of $\gamma_{\text{sae}} = 128$ and $\lambda_{\text{sparse}} = 32$, resulting in a high-dimensional latent space of $512 \times 128 = 65,536$ dimensions. The SVM classifiers are trained and tested on balanced datasets containing 1,000 positive and 1,000 negative samples each. During the inversion process, activation values $h^{(t)}$ are uniformly sampled at 50 time steps between $t = 999$ and $t = 500$, which serve as inputs to the classifiers. The dataset is split into training and testing sets with an 8:2 ratio.

Concepts	top-1	top-2	top-4	top-8	top-16
Smiling	0.671	0.755	0.851	0.948	0.993
Big Nose	0.675	0.694	0.736	0.771	0.818
Young	0.655	0.702	0.757	0.797	0.855
No Beard	0.757	0.825	0.851	0.891	0.929
Blond Hair	0.677	0.750	0.843	0.883	0.938

Table 3. SVM classification accuracy for top- k latent dimensions across different concepts.

Results. Even the single highest-ranked latent unit (top-1) achieves accuracy vastly above the random baseline (50%), confirming that individual CASL-aligned dimensions carry

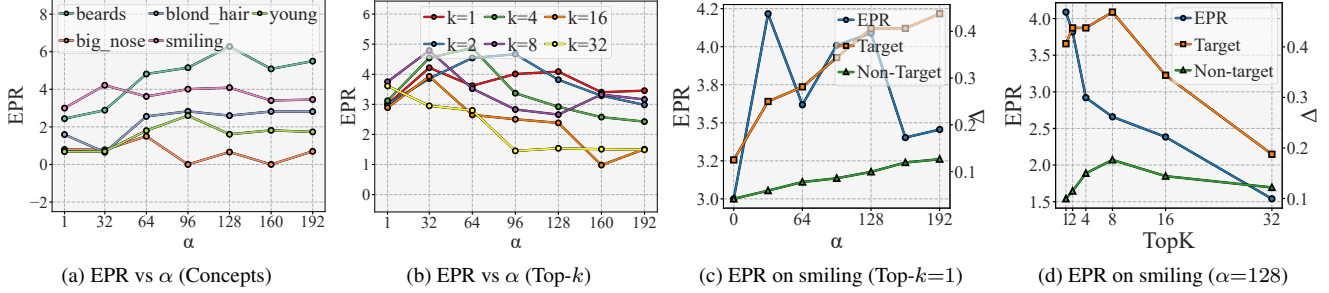


Figure 4. Hyperparameter analysis of editing intensity α and top- k dimension selection. (a) Single-dimension editing shows stable EPR across concepts. (b) Multi-dimension editing reduces precision with increasing α . (c) Target and non-target changes scale proportionally for $k = 1$. (d) Increasing k degrades EPR, confirming sparse editing maximizes interpretability.

strong concept-specific signals. Increasing k further improves accuracy, indicating that additional aligned units contribute complementary semantic cues. Using only 16 latent units per concept, all classifiers approach near-perfect accuracy (> 0.93), demonstrating that the aligned latent space is highly concentrated and semantically coherent. These results validate that CASL effectively isolates concept-relevant latent factors in a compact subset of sparse units.

5.6. Hyperparameter Analysis

To better understand the behavior and robustness of our method, we conduct ablation studies of two key hyperparameters: the number of top- k latent dimensions for editing (Eq. 9), and the editing intensity coefficient α (Eq. 11).

Our results are shown in Fig 4.(a). When only the top-1 latent dimension is edited (Fig. 4a), EPR remains stable across a wide range of α for most concepts. This indicates that our SAE successfully extracts disentangled and interpretable latent factors, amplifying a single direction increases the target attribute without introducing unrelated concepts, even under strong editing. (b) For the *smiling* attribute (Fig. 4b), we observe that EPR is robust to changes in α only for top- k =1. When $k > 1$, EPR decreases significantly as α increases, suggesting that editing multiple latent dimensions simultaneously inevitably entangles additional semantic information and reduces editing precision. (c) Figure 4c further decomposes the editing behavior for *smiling* ($k = 1$). As α increases, both the Δ_{target} (Eq. 12) and $\Delta_{\text{non_target}}$ (Eq. 13) changes rise, but EPR remains nearly constant. This implies that, although overall attribute changes are magnified by stronger editing, the *relative* specificity of the edit (i.e., the ratio between target and side effect) is well preserved due to the high semantic purity of the selected latent dimensions. (d) Finally, Figure 4d explores how EPR and score changes respond to increasing k at a fixed α . As k increases, EPR steadily declines and the gap between target and non-target changes narrows. This supports our design choice that sparsity in editing di-

rections (small k) is crucial for maximizing interpretability and precision in semantic manipulation.

Overall, our method yields purified and accurately aligned latent features, allowing precise semantic editing with minimal change. Editing more latent dimensions, however, introduces entanglement and diminishes editing effectiveness. More results can be found in Appendix.

5.7. Computational Cost

CASL requires training the sparse autoencoder once on U-Net activations. On a single A100 GPU, SAE training takes approximately 6 hours with a memory footprint below 32 GB. The subsequent concept-mapping step is a lightweight linear regression and completes within minutes. CASL-Steer itself adds negligible cost at inference, since it injects a single latent shift during DDIM sampling. Overall, CASL introduces only a one-time offline training cost, and its per-edit overhead is comparable to standard DDIM generation.

6. Conclusion

We introduced CASL, a framework that learns a sparse latent space whose individual dimensions are aligned with human-defined semantic concepts in diffusion models. The resulting representation makes concept-relevant information more explicit and separates it from other latent factors, providing a clearer view of how semantics are organized inside the model. Building on this space, CASL-Steer enables controlled probing of concept influence through simple latent interventions, offering a direct way to examine how specific attributes affect the generative process without modifying the diffusion model itself. We further proposed EPR, a metric that jointly evaluates the intended semantic change and the unintended shifts in non-target attributes, allowing a more balanced assessment of semantic alignment quality. Our experiments show that CASL yields compact and interpretable concept directions, and that CASL-Steer consistently exposes their semantic effects across datasets. We hope these insights encourage further exploration of structured and interpretable latent representations for diffusion mod-

els.

References

- [1] Trenton Bricken, Adly Templeton, Joshua Batson, Brian Chen, and Adam et al. Jermyn. Towards monosemanticity: Decomposing language models with dictionary learning. *Transformer Circuits Thread*, 2023. [2](#)
- [2] Tim Brooks, Aleksander Holynski, and Alexei A Efros. Instructpix2pix: Learning to follow image editing instructions. In *Proceedings of the IEEE/CVF conference on computer vision and pattern recognition*, pages 18392–18402, 2023. [2](#)
- [3] Mingdeng Cao, Xintao Wang, Zhongang Qi, Ying Shan, Xiaohu Qie, and Yinqiang Zheng. Masactrl: Tuning-free mutual self-attention control for consistent image synthesis and editing. In *Proceedings of the IEEE/CVF international conference on computer vision*, pages 22560–22570, 2023. [6, 4, 11](#)
- [4] Yunjey Choi, Youngjung Uh, Jaejun Yoo, and Jung-Woo Ha. Stargan v2: Diverse image synthesis for multiple domains. In *Proceedings of the IEEE/CVF conference on computer vision and pattern recognition*, pages 8188–8197, 2020. [5](#)
- [5] Hoagy Cunningham, Aidan Ewart, Logan Riggs, Robert Huben, and Lee Sharkey. Sparse autoencoders find highly interpretable features in language models. *arXiv preprint arXiv:2309.08600*, 2023. [1, 2](#)
- [6] Jiankang Deng, Jia Guo, Niannan Xue, and Stefanos Zafeiriou. Arcface: Additive angular margin loss for deep face recognition. In *Proceedings of the IEEE/CVF conference on computer vision and pattern recognition*, pages 4690–4699, 2019. [6, 3](#)
- [7] Rohit Gandikota, Joanna Materzyńska, Tingrui Zhou, Antonio Torralba, and David Bau. Concept sliders: Lora adaptors for precise control in diffusion models. In *European Conference on Computer Vision*, pages 172–188. Springer, 2024. [2, 6, 3, 11](#)
- [8] Amir Hertz, Ron Mokady, Jay Tenenbaum, Kfir Aberman, Yael Pritch, and Daniel Cohen-Or. Prompt-to-prompt image editing with cross attention control.(2022). URL <https://arxiv.org/abs/2208.01626>, 3, 2022. [3](#)
- [9] Jack Hessel, Ari Holtzman, Maxwell Forbes, Ronan Le Bras, and Yejin Choi. Clipscore: A reference-free evaluation metric for image captioning. In *Proceedings of the 2021 conference on empirical methods in natural language processing*, pages 7514–7528, 2021. [6](#)
- [10] Jonathan Ho, Ajay Jain, and Pieter Abbeel. Denoising diffusion probabilistic models. *Advances in neural information processing systems*, 33:6840–6851, 2020. [5](#)
- [11] Victor Shea-Jay Huang, Le Zhuo, Yi Xin, Zhaokai Wang, Peng Gao, and Hongsheng Li. Tide: Temporal-aware sparse autoencoders for interpretable diffusion transformers in image generation. *arXiv preprint arXiv:2503.07050*, 2025. [1, 2, 3](#)
- [12] Ayodeji Ijishakin, Ming Liang Ang, Levente Baljer, Daniel Chee Hian Tan, Hugo Laurence Fry, Ahmed Abdulaal, Aengus Lynch, and James H Cole. H-space sparse autoencoders. In *Neurips Safe Generative AI Workshop 2024*, 2024. [1, 2](#)
- [13] Jaeseok Jeong, Mingi Kwon, and Youngjung Uh. Training-free content injection using h-space in diffusion models. In *Proceedings of the IEEE/CVF Winter Conference on Applications of Computer Vision*, pages 5151–5161, 2024. [1](#)
- [14] Tero Karras, Timo Aila, Samuli Laine, and Jaakko Lehtinen. Progressive growing of gans for improved quality, stability, and variation. *arXiv preprint arXiv:1710.10196*, 2017. [5](#)
- [15] Tero Karras, Samuli Laine, and Timo Aila. A style-based generator architecture for generative adversarial networks. In *Proceedings of the IEEE/CVF conference on computer vision and pattern recognition*, pages 4401–4410, 2019. [5](#)
- [16] Bahjat Kawar, Shiran Zada, Oran Lang, Omer Tov, Huiwen Chang, Tali Dekel, Inbar Mosseri, and Michal Irani. Imagic: Text-based real image editing with diffusion models. In *Proceedings of the IEEE/CVF conference on computer vision and pattern recognition*, pages 6007–6017, 2023. [2](#)
- [17] Dahye Kim, Xavier Thomas, and Deepti Ghadiyaram. : Interpreting and leveraging semantic information in diffusion models. *CorRR*, 2024. [2](#)
- [18] Gwanghyun Kim, Taesung Kwon, and Jong Chul Ye. Diffusionclip: Text-guided diffusion models for robust image manipulation. In *Proceedings of the IEEE/CVF conference on computer vision and pattern recognition*, pages 2426–2435, 2022. [2, 4](#)
- [19] Mingi Kwon, Jaeseok Jeong, and Youngjung Uh. Diffusion models already have a semantic latent space. *arXiv preprint arXiv:2210.10960*, 2022. [1, 2, 4, 6, 3, 11](#)
- [20] Chenlin Meng, Yutong He, Yang Song, Jiaming Song, Jianjun Wu, Jun-Yan Zhu, and Stefano Ermon. Sddit: Guided image synthesis and editing with stochastic differential equations. *arXiv preprint arXiv:2108.01073*, 2021. [2](#)
- [21] Trong-Tung Nguyen, Quang Nguyen, Khoi Nguyen, Anh Tran, and Cuong Pham. Swiftedit: Lightning fast text-guided image editing via one-step diffusion. In *Proceedings of the Computer Vision and Pattern Recognition Conference (CVPR)*, pages 21492–21501, 2025. [6, 11](#)
- [22] Alexander Quinn Nichol and Prafulla Dhariwal. Improved denoising diffusion probabilistic models. In *International conference on machine learning*, pages 8162–8171. PMLR, 2021. [5](#)
- [23] Jiaming Song, Chenlin Meng, and Stefano Ermon. Denoising diffusion implicit models, 2022. [2](#)
- [24] Yang Song, Jascha Sohl-Dickstein, Diederik P Kingma, Abhishek Kumar, Stefano Ermon, and Ben Poole. Score-based generative modeling through stochastic differential equations. *arXiv preprint arXiv:2011.13456*, 2020. [5](#)
- [25] Viacheslav Surkov, Chris Wendler, Mikhail Terekhov, Justin Deschenaux, Robert West, and Caglar Gulcehre. Unpacking sdxl turbo: Interpreting text-to-image models with sparse autoencoders. In *Mechanistic Interpretability for Vision at CVPR 2025 (Non-proceedings Track)*, 2025. [1, 2, 3](#)
- [26] Zizheng Yang, Hu Yu, Bing Li, Jinghao Zhang, Jie Huang, and Feng Zhao. Unleashing the potential of the semantic latent space in diffusion models for image dehazing. In *European Conference on Computer Vision*, pages 371–389. Springer, 2024. [1](#)
- [27] Fisher Yu, Ari Seff, Yinda Zhang, Shuran Song, Thomas Funkhouser, and Jianxiong Xiao. Lsun: Construction of a

- large-scale image dataset using deep learning with humans in the loop. *arXiv preprint arXiv:1506.03365*, 2015. 5
- [28] Zhenbo Yu, Jian Jin, Jinhan Zhao, Zhenyong Fu, and Jian Yang. Tfddiffusion: Training-free and text-free image editing in diffusion models with structural and semantic disentanglement. *Neurocomputing*, 619:129159, 2025. 1, 2
 - [29] Richard Zhang, Phillip Isola, Alexei A Efros, Eli Shechtman, and Oliver Wang. The unreasonable effectiveness of deep features as a perceptual metric. In *Proceedings of the IEEE conference on computer vision and pattern recognition*, pages 586–595, 2018. 6, 2
 - [30] Ye Zhu, Yu Wu, Zhiwei Deng, Olga Russakovsky, and Yan Yan. Boundary guided learning-free semantic control with diffusion models. *Advances in Neural Information Processing Systems*, 36:78319–78346, 2023. 1, 2, 6, 4, 11

CASL: Concept-Aligned Sparse Latents for Interpreting Diffusion Models

Supplementary Material

7. Implementation Details

7.1. Code

We provide our code in the supplementary material. Please check.

7.2. Model and Architecture Settings

SAE Training Details. We train the sparse autoencoder (SAE) on cached U-Net bottleneck activations extracted at a fixed timestep t_0 . Each activation $h \in \mathbb{R}^{(HW) \times C}$ is reshaped into $N = HW$ spatial tokens of dimension C . Following prior work on token-level interpretability, we adopt a *token-wise* training scheme: a minibatch of 64 images yields $64 \times N$ training tokens per optimization step, allowing the SAE to fully leverage spatial diversity and substantially increase the number of effective training samples.

We keep both the sparsity weight α fixed during training; no annealing schedule is applied. We did not observe training instability that would require warm-up or staged sparsification.

Architecture. The SAE is a linear encoder–decoder with learnable pre-bias and latent bias:

$$z = \phi(W_\eta(h - b_{\text{pre}}) + b_z), \quad \hat{h} = W_\psi z + b_{\text{pre}},$$

where $W_\eta \in \mathbb{R}^{K \times C}$ and $W_\psi \in \mathbb{R}^{C \times K}$. We use *untied* weights ($W_\psi \neq W_\eta^\top$), as tying the decoder noticeably reduces reconstruction fidelity at large expansion ratios. The latent dimension is set to $K = C \cdot \text{scale}$ with $\text{scale} = 32$. We adopt ReLU in our main experiments due to its training stability and smoother gradients.

Timestep Embedding. We keep the timestep embedding enabled (`ignore_timesteps = False`) so that the SAE can capture mild temporal variation in U-Net activations between denoising timesteps $t \in [500, 999]$. Although this temporal variation is limited, we find that including timestep information slightly improves reconstruction accuracy without affecting sparsity or alignment.

Objective. The training objective follows:

$$\mathcal{L} = \|\hat{h} - h\|_2^2 + \lambda_{\text{sparse}} \cdot \|z\|_1,$$

where the sparsity loss is implemented as the mean absolute activation of z . We tune λ_{sparse} to balance reconstruction fidelity and latent sparsity.

To validate the generalizability of our sparse autoencoder, we further conduct ablation studies on the **FFHQ dataset**. As shown in Table 5, we report the reconstruction quality (MSE, Cosine Similarity) and sparsity (DAR, $\tau = 0.01$) under different sparsity loss weights λ_{sparse} , with

the latent dimension γ_{sae} fixed at 128. Compared to the results on CelebA-HQ (see main text), the trends on FFHQ are consistent, demonstrating the robustness of our method across datasets.

Optimization. The SAE is trained for 100 epochs using Adam (learning rate $1\text{r_sae} = 5 \times 10^{-4}$, weight decay disabled). We use a batch size of 64 images (expanded to $64 \times HW$ latent tokens per step). Gradient updates are performed on all tokens jointly, and model checkpoints are saved every 10 epochs. This token-wise design enables efficient large-scale SAE training while maintaining high reconstruction accuracy and strong sparsity.

7.3. Stage-2: Concept Alignment MLP

To map the sparse latent representation to the activation direction for semantic editing, we use a simple linear transformation implemented as a single-layer perceptron:

$$\Delta h = W_\Delta z + b_\Delta$$

where z is the latent vector, W_Δ and b_Δ are learnable parameters, and Δh is the predicted direction in the activation space.

This operation is implemented in PyTorch as:

```
1 import torch.nn as nn
2
3 direction_decoder = nn.Linear(latent_dim,
4                               out_dim)
4 delta_h = direction_decoder(z)
```

7.4. Steering Pipeline.

We apply semantic intervention during the denoising trajectory of the U-Net. Let $t_{\text{edit}} = 500$ denote the editing threshold. Following DDIM inversion, we obtain the noisy trajectory $\{x_t\}_{t=999}^0$ and at each denoising step we extract the bottleneck activation h_t from the middle block.

Timestep-wise intervention. Editing is applied not at a single timestep, but repeatedly across the range $t \in [500, 999]$. At every denoising step satisfying $t \geq t_{\text{edit}}$, we modify the bottleneck activation through a concept-aligned shift:

$$h'_t = h_t + \gamma \Delta h_c, \quad \Delta h_c = W_\Delta z_t,$$

where z_t is the sparse latent representation produced by the SAE encoder, and W_Δ is the concept-mapping linear layer from Stage 2. Only this middle-block activation is modified; all other layers and all timesteps $t < 500$ remain unchanged.

Continuation of sampling. The modified activation h'_t is injected via a forward hook and the remaining DDIM up-

date is computed normally:

$$x_{t-1} = \sqrt{\alpha_{t-1}} P_t(\epsilon_\theta(x_t | h'_t)) + D_t(\epsilon_\theta(x_t)).$$

Since the intervention is applied across roughly 50 denoising steps (using a step size of 10 from $t = 999$ to $t = 500$), the influence of the concept-aligned shift accumulates smoothly along the trajectory, enabling controlled semantic modification without altering the early generative dynamics.

7.5. Layer Selection for h -space in U-Net

Following prior work [19], we define the h -space as the intermediate feature representation at the bottleneck layer of the U-Net architecture. Specifically, we select the 8th layer (with spatial resolution 8×8 and channel dimension 512) as our h -space. This layer is not directly influenced by skip connections, which ensures that the activations encode high-level and abstract semantics, making it suitable for both sparse autoencoding and concept editing.

Our choice is motivated by the comprehensive empirical analysis in [19], where the authors systematically evaluated semantic editing performance at different layers of the U-Net. Their experiments demonstrated that the bottleneck layer (layer 8) contains the richest and most disentangled semantic information, and editing this layer yields the most effective and interpretable results for semantic manipulation tasks.

7.6. Hyperparameter Selection for Training Loss.

The selection of hyperparameters for CLIP loss (Eq. 8) is crucial for achieving optimal semantic alignment and faithful reconstruction in semantic editing tasks. As shown in Table 4, we empirically select the weighting factors for the CLIP loss and reconstruction loss ($\lambda_{\text{CLIP}} : \lambda_{\text{recons}}$) based on experiments and prior work, tailoring the settings to different datasets and target concepts. For each dataset (e.g., CelebA-HQ, FFHQ, LSUN-Church, AFHQ-Dog), we consider multiple representative concepts and adjust the loss weights accordingly to balance the semantic editing strength and image fidelity. Table 4 summarizes the datasets, concepts, target descriptions, and corresponding hyperparameter configurations used in our experiments.

7.7. Datasets and Preprocessing

Datasets and Preprocessing

AFHQ. We use the AFHQ-Dog subset following prior diffusion editing literature. Images are loaded from the official train/test split (`train/dog/*.png`, `test/dog/*.png`). Each image is resized to $s \times s$ (where s is the target resolution for each backbone, e.g., 256 or 512), converted to a float tensor in $[0, 1]$, and normalized to $[-1, 1]$ using a standard `ToTensor` +

`Normalize((0.5, 0.5, 0.5), (0.5, 0.5, 0.5))` transform. No data augmentation is applied to preserve the deterministic nature of DDIM inversion.

CelebA-HQ. CelebA-HQ is stored in LMDB format for efficient random access. Each sample is retrieved via a resolution-specific LMDB key `'<res>-<index>'`, decoded into a JPEG/PNG image, and processed with the same normalization described above. The LMDB files contain the official train and test partitions. All images are resized to the target model resolution and transformed with `ToTensor` and `Normalize` without augmentation.

LSUN-Church. For LSUN, we adopt the official LMDB release and follow the conventional train/validation split (`church_outdoor_train`, `church_outdoor_val`). The loader retrieves each image from LMDB, converts it to RGB, applies `Resize` and `CenterCrop` to match the desired resolution, and then normalizes it to the $[-1, 1]$ range. The same preprocessing is applied to both training and test images.

Normalization. Across all datasets, images are scaled to $[-1, 1]$, which matches the input range expected by the U-Net denoisers used in DDPM/DM/SDXL models. We avoid augmentation because diffusion inversion and semantic editing require consistent reconstruction of the original image.

7.8. Metrics

Editing Precision Ratio (EPR). For EPR, we use the classifier *logits* rather than probabilities, as logits preserve relative semantic strength without saturation effects. We set $\epsilon = 10^{-8}$ purely for numerical stability; this does not affect the scale or ranking of the metric. For each target attribute c , all remaining annotated attributes in the dataset are treated as non-target attributes. This design evaluates unintended changes across the full attribute space, and datasets with rich attribute annotations (e.g., CelebA-HQ with 40+ labels) provide more reliable and discriminative EPR estimates.

Learned Perceptual Image Patch Similarity (LPIPS).

We evaluate perceptual distortion using LPIPS [29]. Following the official implementation, we adopt the AlexNet-based LPIPS model (`lpips.LPIPS(net='alex')` in our code). All images are resized to the target resolution and normalized to the $[-1, 1]$ range before evaluation. Given an original image x and its edited counterpart \hat{x} , LPIPS computes the L_2 distance between deep features extracted from a pretrained perceptual network. Lower LPIPS indicates better preservation of non-target visual details.

CLIP-Score. To measure the semantic alignment between the edited images and the target attribute, we compute CLIP-Score using the ViT-L/14 CLIP model. For a text prompt t describing the target attribute, the CLIP encoder extracts a normalized text representation f_t , and each edited image \hat{x} is mapped to a normalized visual feature $f_{\hat{x}}$. The CLIP-Score is the cosine similarity

$$\text{CLIP}(\hat{x}, t) = \langle f_{\hat{x}}, f_t \rangle,$$

where higher scores indicate stronger semantic consistency with the target attribute. All images are normalized using the default CLIP preprocessing pipeline, and scores are averaged over the entire evaluation set.

ArcFace Similarity. To quantify identity preservation in face-editing experiments, we compute the cosine similarity between ArcFace embeddings of the original and edited images. Following the standard InsightFace implementation [6], each face is detected and aligned using the SCRFD detector, and a 512-dimensional normalized embedding is extracted by the `buffalo_1` model (ResNet-50 backbone).

Given two embeddings $e, \hat{e} \in \mathbb{R}^{512}$, identity similarity is

$$\text{Sim}(e, \hat{e}) = \frac{\langle e, \hat{e} \rangle}{\|e\|_2 \|\hat{e}\|_2} \in [0, 1],$$

where higher values indicate stronger identity consistency. Images are evaluated after automatic face alignment, and pairs with undetected faces are excluded, following common practice in prior work.

7.9. Baseline Configuration

7.9.1. Concept Sliders

We implement Concept Sliders [7] as our baseline method for controllable image editing. The baseline configuration follows the original implementation with the following specifications:

Model Architecture. We use Stable Diffusion v1.4 as the base diffusion model with LoRA adaptation for concept manipulation. The LoRA network employs a `c31ier` architecture targeting both linear and convolutional layers in the UNet, with rank $r = 4$ and scaling factor $\alpha = 1.0$. Training is performed using the `noxattn` method, excluding cross-attention layers from adaptation.

Training Configuration. The model is trained for 1,000 iterations using the AdamW optimizer with a constant learning rate of 2×10^{-4} . We use DDIM scheduling with 50 denoising steps and classifier-free guidance scale of 4.0. All training is conducted at 512×512 resolution with bfloat16 precision.

Concept Definitions. For each target attribute, we define concept pairs using natural language prompts:

- **Smiling:** “smiling person” vs. “sad person”
- **Big Nose:** “person with big nose” vs. “person with small nose”
- **Beards:** “person with beards” vs. “person without beards”
- **Blonde Hair:** “person with blonde hair” vs. “person without blonde hair”
- **Young:** “very young person” vs. “very old person”

All concepts use “person” as the neutral anchor point for conditioning.

Inference Protocol. During inference, we apply the trained LoRA weights with editing strength $\alpha \in \{1, 32, 64, 96, 128\}$ using DDIM sampling with 50 steps. The LoRA scaling is activated after timestep 500 to preserve image fidelity while enabling concept manipulation. We use classifier-free guidance with scale 7.5 and the prompt “a photo of a person” for all evaluations.

Implementation Details. Models are implemented using the Diffusers library and trained on NVIDIA A100 GPUs. LoRA weights are saved every 500 iterations, with the final checkpoint used for evaluation. All images are processed at 512×512 resolution with standard normalization.

7.9.2. Asyrp

We implement Asyrp [19] as another baseline method for semantic image editing. Asyrp performs editing by learning delta blocks that modify intermediate features in the diffusion denoising process at specific timesteps.

Model Architecture. The method uses a pre-trained diffusion model on CelebA-HQ with a simple UNet architecture. The UNet consists of 128 base channels with channel multipliers $[1, 1, 2, 2, 4, 4]$, 2 residual blocks per resolution, and self-attention at 16×16 resolution. All processing is performed at 256×256 resolution with 3 input/output channels.

Diffusion Configuration. The diffusion process employs a linear noise schedule with $\beta_{\text{start}} = 10^{-4}$, $\beta_{\text{end}} = 0.02$, and $T = 1000$ timesteps. Sampling uses DDIM with 50 denoising steps during both training and inference.

Training Protocol. Delta blocks are trained using 100 training images and 32 test images over 5 iterations with batch size 1. The learning rate is set to 0.5 with a combined loss function:

$$\mathcal{L} = \lambda_{\text{CLIP}} \mathcal{L}_{\text{CLIP}} + \lambda_{L1} \mathcal{L}_{L1} \quad (16)$$

where $\lambda_{\text{CLIP}} = 1.0$ and $\lambda_{L1} = 3.0$. Training employs 50 DDIM inversion steps (n_{inv}) and 50 generation steps (n_{train}).

Temporal Control. The method uses adaptive timestep selection based on LPIPS distance thresholds:

- **Edit timestep** $t_{\text{edit}} = 500$: when delta blocks begin activation
- **LPIPS thresholds**: $\tau_{\text{edit}} = 0.33$, $\tau_{\text{noise}} = 0.1$ for automatic timestep determination

Concept Definitions. Semantic concepts are defined using text prompt pairs from source to target:

- **Smiling**: “face” → “smiling face”
- **Big Nose**: “person” → “person with big nose”
- **Beards**: “person” → “person with beards”
- **Blonde Hair**: “person” → “person with blond hair”
- **Age**: “person” → “young person” / “old person”

Inference Procedure. During inference, the method follows a three-stage process: (1) DDIM inversion with 50 steps to obtain latent codes, (2) forward diffusion with delta block injection starting at t_{edit} , and (3) optional noise injection from t_{noise} using the `add_noise_from_xt` strategy. The editing strength is controlled by the coefficient $\alpha = 1.0$.

7.9.3. BoundaryDiffusion.

We include BoundaryDiffusion [30] as a representative classifier-guided editing baseline. For each semantic attribute, we use the official CLIP-based boundaries provided by the authors, which contain both activation-space boundaries (W_h) and latent-space boundaries (W_z). During editing, the U-Net activation at timestep $t = 500$ is perturbed along the attribute direction by traversing the boundary over a fixed range ($[-500, 500]$ in our implementation), following the protocol in the original work. All methods use the same DDIM inversion setup ($n_{\text{inv}} = 40$ steps) and the same number of forward editing steps ($n_{\text{edit}} = 40$). The boundary is applied only once per denoising step, and all other hyperparameters are kept identical to the official implementation for fair comparison.

7.9.4. MasaCtrl

We employ MasaCtrl [3] as a baseline method. This approach achieves structure-preserving image editing by controlling the mutual self-attention mechanism within the U-Net architecture of diffusion models. Our configuration uses Stable Diffusion v1.4 as the pre-trained foundation model with a DDIM scheduler for the denoising process, setting `beta_start=0.00085`, `beta_end=0.012`, and `beta_schedule="scaled_linear"`. The MasaCtrl control parameters are configured as follows: `start_step=4`, `start_layer=10`, `total_inference_steps=50`, and `guidance_scale=7.5`. The method first performs DDIM inversion to map the source image into the latent space, then applies mutual self-attention control during specified denoising steps (4-50) and U-Net layers (10-16) to

achieve semantic editing while preserving structural coherence. Image preprocessing includes resizing input images to 512×512 resolution and normalizing pixel values to the $[-1, 1]$ range. To ensure reproducibility, we set fixed random seeds for each image during the editing process.

7.9.5. SwiftEdit:

We employ SwiftEdit as a baseline method for lightning-fast text-guided image editing via one-step diffusion. SwiftEdit utilizes a pre-trained diffusion model with single-step inversion and sampling to achieve significant efficiency improvements. Our configuration includes: image resolution resized to 512×512 pixels, middle timestep $t_{\text{mid}} = 500$, and final timestep $t_{\text{final}} = 999$. The mask generation parameters are set as follows: text hidden state scaling factor $\alpha_{ta} = 1$, editing region scaling factor $\alpha_{\text{edit}} = 0.2$, non-editing region scaling factor $\alpha_{\text{non-edit}} = 1$, mask threshold $\tau_{\text{mask}} = 0.5$, and clamp rate $\gamma_{\text{clamp}} = 3.0$. The method first predicts inverted noise through the inverse U-Net, then estimates editing masks based on the difference between source and edit prompts, and finally applies mask controllers at specified U-Net layers (“mid_blocks” and “up_blocks”) for localized editing.

7.10. Choice of α in Different Concepts

The hyperparameter α determines the editing intensity along each semantic direction. In our experiments, the value of α for each concept is primarily chosen based on visual inspection of the editing results on the validation set. Specifically, we adjust α to achieve a balance between perceptible attribute change and preservation of image realism. Notably, for attributes that are abundant in the dataset (e.g., *smiling* in CelebA-HQ), a smaller α is typically sufficient to induce clear semantic changes, whereas less common or more subtle attributes often require a larger value of α . The final α settings for all datasets and concepts are summarized in Table 6.

We do not rely on the Editing Precision Ratio (EPR) metric for the selection of α due to two primary limitations. First, EPR can only be computed on datasets with explicit attribute annotations (e.g., CelebA-HQ), restricting its applicability to many datasets or concepts without such labels. Second, EPR is inherently limited to the predefined set of annotated attributes, and therefore fails to capture editing quality for concepts or semantic directions that are not covered by existing labels. In contrast, visual inspection enables a more comprehensive and flexible assessment of editing performance across diverse and potentially unannotated attributes.

8. User Study Design

To further evaluate the effectiveness of our Editing Precision Ratio (EPR) metric, we conducted a user study to as-

Dataset	Concept	y^{origin}	y^{ref}	$\lambda_{\text{CLIP}} : \lambda_{\text{recons}}$
CelebA-HQ	Smiling	face	smiling face	3:1
	Big Nose	person	person with big nose	3:1
	Blond Hair	person	person with blond hair	3:1
	Beards	person	person with beards	3:1
	Eyeglasses	person	person wearing eyeglasses	3:1
	Narrow eyes	face	face with narrow eyes	3:1
	arched eyebrow	face	face with arched eyebrows	3:1
	Young	person	young person	3:1
FFHQ	Beards	person	person with beards	3:1
	Young	person	young person	3:1
	tanned	face	tanned face	3:1
	angry	face	angry face	3:1
	sad	face	sad face	3:1
LSUN-Church	Gothic	Church	Gothic Church	2.5:1
	Red Brick	Church	Red brick wall Church	2.5:1
	Snowy	Church	snowy day	2.5:1
	wooden	Church	Wooden House	2.5:1
AFHQ-Dog	Angry	Dog	Angry Dog	2.2:1
	Sleepy	Dog	Sleepy Dog	2.2:1
	Smiling	Dog	Smiling Dog	2.2:1
	puppy	Dog	Puppy	2.2:1

Table 4. Hyperparameter settings for CLIP loss and reconstruction loss for different datasets and concepts.

Params	MSE \downarrow	Cosine Sim. \uparrow	DAR ($\tau = 0.01$) \downarrow
$\lambda_{\text{sparse}} = 0.5$	2.34×10^{-2}	0.993	2.72×10^{-2}
$\lambda_{\text{sparse}} = 1$	2.33×10^{-2}	0.994	2.50×10^{-2}
$\lambda_{\text{sparse}} = 2$	2.18×10^{-2}	0.994	2.23×10^{-2}
$\lambda_{\text{sparse}} = 4$	2.07×10^{-2}	0.994	2.03×10^{-2}
$\lambda_{\text{sparse}} = 8$	2.30×10^{-2}	0.993	1.80×10^{-2}
$\lambda_{\text{sparse}} = 16$	2.77×10^{-1}	0.987	4.81×10^{-2}
$\lambda_{\text{sparse}} = 32$	3.69×10^{-1}	0.986	1.72×10^{-2}

Table 5. Reconstruction quality and sparsity of the SAE trained on FFHQ across different sparsity loss weight λ_{sparse} .

sess whether the metric aligns with human perception of editing quality.

8.1. Experimental Setup

In this experiment, we invited **10** participants to rate a collection of edited images generated by different semantic editing methods, including ours and baseline approaches. Each test sample consists of the following:

- **Original Image:** The unedited reference image.
- **Target Description:** The semantic attribute to be edited (e.g., “smiling”).
- **Edited Image:** The result of semantic editing according to the target attribute.

For each sample, participants were instructed to evaluate the edited image on two aspects:

Dataset	Concept	α
CelebA-HQ	Smiling	128
	Big Nose	64
	Blond Hair	128
	Beards	96
	Eyeglasses	96
	Narrow eyes	160
	arched eyebrow	160
	Young	128
FFHQ	Beards	96
	Young	128
	tanned	80
	angry	80
	sad	64
LSUN-Church	Gothic	16
	Red Brick	16
	Snowy	16
	wooden	16
AFHQ-Dog	Angry	32
	Sleepy	64
	Smiling	31
	puppy	64

Table 6. Hyperparameter settings for α for different datasets and concepts.

1. **Target Change:** How much does the edited image match the target description?
(1 = No visible change, 10 = Completely matches the target description)
 2. **Identity Preservation:** How well does the edited image preserve the identity of the original image?
(1 = Perfectly preserves identity, 10 = Looks like a completely different person/image)
- Participants were asked to provide their ratings in the format: **Target/Non-target** (e.g., 3/2).

8.2. Procedure

The method names and editing settings were anonymized to ensure a fair assessment. Prior to the formal study, a brief tutorial and several examples were given to each participant.

8.3. Participants

A total of **10** participants were recruited for the user study. (Details of participant demographics are omitted for anonymity.)

8.4. Results

Detailed results are provided in the supplementary file `Human_Evaluation.pdf`. We further observe that the trends in human evaluation are largely aligned with those measured by the EPR metric, demonstrating the rationality and practical effectiveness of our approach.

8.5. Summary

This user study aims to assess the subjective perception of editing precision and identity preservation, and to validate the consistency between the EPR metric and human judgment.

9. Performance of the Attribute Classifier

To ensure fair and robust evaluation, we independently trained four attribute classifiers, ResNet18, VGG16, MobileNetV2, and ViT-B/16, using identical settings on the **cropped CelebA** dataset. All classifiers are fine-tuned from ImageNet-pretrained weights.

Following the standard protocol, we split the dataset as follows: images with indices `image_n < 162771` are used for training, $162771 \leq \text{image}_n < 182638$ for validation, and `image_n ≥ 182638` for testing.

- **ResNet18** is a classical convolutional neural network (CNN) featuring residual connections, which enable effective training of deep models by mitigating the vanishing gradient problem.
- **VGG16** is a deep CNN characterized by its uniform use of 3×3 convolutional layers and simple, sequential architecture, widely adopted as a strong baseline for visual tasks.

- **MobileNetV2** is a lightweight CNN designed for efficient inference on mobile and embedded devices, employing depthwise separable convolutions and inverted residual blocks to reduce computational cost while maintaining competitive performance.
- **ViT-B/16** is a vision transformer model that processes images as sequences of non-overlapping patches and leverages self-attention mechanisms to capture global dependencies, marking a departure from traditional CNN-based designs.

The tables below (table. 7, table. 8, table. 9, table. 10) reports their performance on the test set. As shown, all classifiers achieve consistently high accuracy, demonstrating stable and reliable attribute prediction across different initializations.

9.1. Ablation Study on EPR Sensitivity

To better understand the behavior and limitations of the Editing Precision Ratio (EPR), we conduct an ablation study using different attribute classifiers, including ResNet18, MobileNetV2, VGG16, and ViT-B/16. The results are summarized in Table 11, which reports EPR for five facial attributes across all editing methods.

Overall, EPR values exhibit substantial variation across classifier backbones. For example, the same edited images can yield noticeably different EPR scores when evaluated by ResNet18 versus VGG16, and ViT-B/16 shows an even larger degree of inconsistency, often producing unstable or uninformative scores. This divergence indicates that EPR is highly sensitive to the choice of attribute classifier: models with different architectures, feature embeddings, and decision boundaries respond differently to subtle attribute shifts introduced during editing.

While EPR provides a convenient quantitative measure of editing specificity under supervised attribute labels, this ablation highlights several inherent limitations. First, EPR fundamentally depends on high-quality, concept-aligned labels, and cannot be reliably computed when labels are noisy, ambiguous, or unavailable. Second, its dependence on a particular classifier introduces model-induced bias, making absolute EPR values difficult to compare across backbones or datasets. Finally, concepts with broader visual variation or weak label definitions tend to produce more volatile EPR scores, limiting the metric's robustness in open-domain or attribute-sparse settings.

Taken together, these findings suggest that EPR should be interpreted with caution and primarily as a relative metric within a fixed classifier setting, rather than as an absolute measure of editing quality. This motivates the need for complementary evaluation metrics, such as CLIP-Score and LPIPS, that do not rely on explicit attribute labels or classifier decision boundaries.

Attribute	Accuracy	Balanced Acc	F1	Precision	Recall
5_o_Clock_Shadow	94.823	86.954	74.849	72.718	77.121
Arched_Eyebrows	84.358	80.833	72.543	72.449	72.656
Attractive	83.173	83.163	82.846	83.766	81.962
Bags_Under_Eyes	85.504	78.772	65.342	63.375	67.451
Bald	99.067	86.849	77.095	80.376	74.090
Bangs	96.204	91.944	87.557	89.435	85.757
Big_Lips	72.832	62.683	44.509	67.068	33.346
Big_Nose	84.297	76.823	63.289	62.761	63.847
Black_Hair	90.484	86.472	81.599	85.930	77.687
Blond_Hair	96.182	91.368	85.547	86.308	84.805
Blurry	96.380	73.442	57.232	71.188	47.921
Brown_Hair	89.496	83.691	71.858	69.291	74.631
Bushy_Eyebrows	93.038	80.330	70.158	78.885	63.179
Chubby	95.942	75.738	58.131	64.195	53.138
Double_Chin	96.470	72.727	54.690	66.250	46.594
Eyeglasses	99.684	98.401	97.541	98.162	96.928
Goatee	97.593	88.127	74.747	72.023	77.705
Gray_Hair	98.296	84.933	72.536	74.555	70.660
Heavy_Makeup	92.040	91.481	90.008	91.535	88.538
High_Cheekbones	88.085	87.996	87.370	89.293	85.529
Male	98.373	98.214	97.887	98.261	97.517
Mouth_Slightly_Open	94.339	94.332	94.241	94.938	93.555
Mustache	97.112	72.738	55.364	68.804	46.321
Narrow_Eyes	87.750	64.538	43.325	69.442	31.503
No_Beard	96.516	93.404	97.956	98.109	97.804
Oval_Face	76.107	63.041	43.454	72.329	31.079
Pale_Skin	97.200	75.297	60.674	74.176	51.381
Pointy_Nose	77.812	68.238	54.168	66.095	45.898
Receding_Hairline	94.025	74.910	59.570	69.943	51.889
Rosy_Cheeks	95.408	77.371	63.751	73.512	56.313
Sideburns	97.952	89.587	78.453	76.631	80.367
Smiling	93.365	93.366	93.268	94.721	91.859
Straight_Hair	84.999	74.687	61.427	66.734	56.912
Wavy_Hair	85.321	82.027	77.616	87.235	69.911
Wearing_Earrings	90.660	86.182	77.657	76.787	78.550
Wearing_Hat	99.176	94.328	90.086	91.165	89.035
Wearing_Lipstick	94.172	94.236	94.322	95.931	92.768
Wearing_Necklace	88.140	65.181	43.759	63.258	33.476
Wearing_Necktie	97.088	87.067	78.399	81.664	75.411
Young	89.021	82.631	92.913	90.866	95.056
Cumulative avg	91.712	86.739	81.218	85.327	77.487
Attr avg mean	91.712	82.353	73.193	78.754	69.754

Table 7. Performance of ResNet-18 attribute classifier on CelebA (test set).

10. Additional Results

10.1. Quantitative Results

To further examine the generalization ability of our method beyond human facial attributes, we additionally evaluate it

on two structurally different datasets: LSUN-Church and AFHQ-Dog. For LSUN-Church, we consider four architectural concepts (Gothic, Red Brick, Snowy, Wooden), while AFHQ-Dog includes four canine appearance and expression traits (Angry, Sleepy, Smiling, Puppy-like). The cor-

Attribute	Accuracy	Balanced Acc	F1	Precision	Recall
5_o_Clock_Shadow	91.705	78.454	63.491	66.067	61.109
Arched_Eyebrows	80.717	75.203	63.096	62.417	63.790
Attractive	77.224	77.149	78.298	77.602	79.007
Bags_Under_Eyes	80.717	68.110	50.046	54.087	46.566
Bald	98.374	73.924	55.201	64.194	48.418
Bangs	94.166	87.406	79.656	81.560	77.839
Big_Lips	78.140	60.898	33.563	31.406	36.038
Big_Nose	79.061	68.338	52.759	60.135	46.996
Black_Hair	89.681	85.422	75.950	73.904	78.113
Blond_Hair	94.458	88.492	81.598	83.396	79.876
Blurry	94.956	64.091	36.015	45.048	30.000
Brown_Hair	83.843	75.279	63.688	69.558	58.731
Bushy_Eyebrows	90.985	78.912	66.227	71.036	62.028
Chubby	94.196	66.582	42.551	53.982	35.115
Double_Chin	95.520	68.609	45.930	56.334	38.769
Eyeglasses	98.102	90.551	85.714	90.048	81.779
Goatee	95.012	78.792	63.845	68.520	59.768
Gray_Hair	97.448	82.861	71.786	77.711	66.701
Heavy_Makeup	89.435	88.979	86.520	86.138	86.905
High_Cheekbones	85.755	85.560	84.065	84.503	83.632
Male	97.443	97.404	97.001	96.864	97.139
Mouth_Slightly_Open	91.307	91.292	90.969	91.079	90.860
Mustache	95.435	68.332	45.786	57.164	38.185
Narrow_Eyes	91.101	68.001	40.790	40.763	40.818
No_Beard	93.104	87.510	95.823	95.462	96.187
Oval_Face	71.702	61.514	43.155	49.341	38.347
Pale_Skin	96.341	71.982	51.630	59.969	45.327
Pointy_Nose	72.769	63.140	46.030	52.864	40.760
Receding_Hairline	93.321	71.419	49.678	54.222	45.836
Rosy_Cheeks	94.438	73.303	54.545	61.789	48.822
Sideburns	95.616	78.372	64.694	72.545	58.376
Smiling	90.915	90.872	90.504	91.443	89.586
Straight_Hair	79.856	66.129	46.640	51.215	42.815
Wavy_Hair	80.284	77.555	66.718	62.576	71.447
Wearing_Earrings	84.945	73.431	58.139	61.889	54.817
Wearing_Hat	98.294	89.652	81.626	83.204	80.106
Wearing_Lipstick	91.136	91.412	90.435	87.164	93.962
Wearing_Necklace	86.420	58.067	26.883	38.331	20.701
Wearing_Necktie	95.319	79.017	65.038	71.076	59.945
Young	84.728	76.719	90.088	87.388	92.961
Cumulative avg	89.349	83.781	75.443	77.189	73.774
Attr avg mean	89.349	76.968	64.404	68.100	61.704

Table 8. Performance of ViT-B/16 attribute classifier on CelebA (test set).

responding quantitative comparisons are presented in Table 12 and Table 13. Across both datasets, our approach produces stable and semantically aligned edits while maintaining distortion levels comparable to, or lower than, existing editing baselines. These observations suggest that

the sparse latent directions learned by our method capture concept-level semantics that transfer reasonably well across diverse visual domains.

It is important to note that we do not report EPR or ArcFace on these datasets. EPR is specifically designed for set-

Attribute	Accuracy	Balanced Acc	F1	Precision	Recall
5_o_Clock_Shadow	94.357	84.224	74.803	79.087	70.959
Arched_Eyebrows	86.339	82.280	73.650	73.422	73.880
Attractive	81.985	81.930	82.786	82.283	83.295
Bags_Under_Eyes	84.240	73.585	59.311	63.850	55.375
Bald	99.018	83.899	74.172	81.395	68.127
Bangs	95.898	91.404	85.883	86.739	85.043
Big_Lips	82.020	65.167	41.056	41.247	40.867
Big_Nose	83.480	74.608	63.173	70.925	56.949
Black_Hair	91.710	87.876	80.358	79.439	81.298
Blond_Hair	95.777	91.226	86.047	87.487	84.653
Blurry	96.653	74.839	58.925	70.250	50.745
Brown_Hair	86.067	78.005	68.373	75.575	62.424
Bushy_Eyebrows	92.742	81.615	72.173	79.541	66.054
Chubby	95.767	74.029	58.754	72.783	49.260
Double_Chin	96.703	74.484	59.742	74.540	49.846
Eyeglasses	99.577	97.967	96.937	97.792	96.095
Goatee	96.869	86.584	77.817	81.418	74.522
Gray_Hair	97.966	85.636	77.506	83.957	71.975
Heavy_Makeup	92.576	92.321	90.549	89.944	91.162
High_Cheekbones	88.312	88.107	86.874	87.677	86.086
Male	98.812	98.791	98.606	98.559	98.652
Mouth_Slightly_Open	94.151	94.138	93.922	94.060	93.785
Mustache	96.275	73.778	56.927	68.392	48.754
Narrow_Eyes	93.467	74.822	54.868	57.009	52.882
No_Beard	96.215	93.322	97.701	97.594	97.809
Oval_Face	75.940	64.326	46.889	61.426	37.916
Pale_Skin	96.909	72.726	56.330	72.000	46.262
Pointy_Nose	77.324	68.244	54.222	63.812	47.138
Receding_Hairline	94.604	76.338	59.455	64.691	55.003
Rosy_Cheeks	95.248	74.830	59.554	71.209	51.178
Sideburns	97.347	87.059	79.582	84.596	75.128
Smiling	93.270	93.230	92.967	93.921	92.033
Straight_Hair	85.423	73.915	60.534	68.275	54.370
Wavy_Hair	86.661	85.155	77.230	73.156	81.783
Wearing_Earrings	91.800	84.555	77.214	82.143	72.842
Wearing_Hat	99.034	94.286	89.711	90.389	89.043
Wearing_Lipstick	92.948	93.290	92.424	88.716	96.456
Wearing_Necklace	89.545	65.786	44.301	61.965	34.474
Wearing_Necktie	96.879	85.543	77.088	82.581	72.280
Young	88.237	81.305	92.369	89.559	95.361
Cumulative avg	91.954	87.354	81.342	83.727	79.088
Attr avg mean	91.954	82.131	73.270	78.085	69.794

Table 9. Performance of MobileNetV2 attribute classifier on CelebA (test set).

tings where each concept is associated with well-defined attribute labels; however, LSUN-Church and AFHQ-Dog do not provide reliable per-image attribute annotations, making EPR ill-defined in these domains. Furthermore, ArcFace is a face recognition model and does not apply to non-human

subjects such as buildings or animals. We therefore limit our evaluation to CLIP-Score and LPIPS, which remain applicable and provide a consistent measure of semantic alignment and perceptual distortion across a broader range of concepts.

Attribute	Accuracy	Balanced Acc	F1	Precision	Recall
5_o_Clock_Shadow	94.378	86.009	75.911	76.789	75.053
Arched_Eyebrows	86.636	83.007	74.488	73.507	75.497
Attractive	81.980	81.878	82.973	81.569	84.427
Bags_Under_Eyes	84.633	74.648	60.854	64.519	57.583
Bald	99.039	88.911	77.126	75.943	78.346
Bangs	96.099	92.587	86.826	86.051	87.616
Big_Lips	84.799	64.574	41.654	50.563	35.414
Big_Nose	83.500	74.060	62.503	71.914	55.270
Black_Hair	91.856	89.017	81.169	78.395	84.146
Blond_Hair	95.666	92.138	86.070	85.120	87.042
Blurry	96.688	77.385	61.565	68.264	56.064
Brown_Hair	86.228	79.327	69.808	74.092	65.992
Bushy_Eyebrows	92.898	83.223	73.661	78.108	69.693
Chubby	95.938	75.927	61.553	73.160	53.125
Double_Chin	96.814	77.071	62.961	73.297	55.179
Eyeglasses	99.562	98.159	96.844	97.162	96.529
Goatee	96.920	88.906	79.184	78.862	79.508
Gray_Hair	98.117	88.561	80.128	82.404	77.973
Heavy_Makeup	92.767	92.692	90.878	89.453	92.349
High_Cheekbones	88.544	88.360	87.160	87.784	86.545
Male	98.822	98.806	98.618	98.536	98.699
Mouth_Slightly_Open	94.403	94.382	94.170	94.527	93.816
Mustache	96.371	76.141	59.878	67.758	53.639
Narrow_Eyes	93.532	78.983	58.959	56.315	61.863
No_Beard	96.421	93.647	97.827	97.704	97.950
Oval_Face	76.408	64.036	46.021	64.080	35.903
Pale_Skin	96.950	75.369	59.383	69.654	51.752
Pointy_Nose	77.425	68.240	54.202	64.215	46.890
Receding_Hairline	94.770	77.525	61.217	65.600	57.383
Rosy_Cheeks	95.138	77.466	61.575	66.955	56.996
Sideburns	97.297	89.369	80.322	80.470	80.176
Smiling	93.628	93.586	93.336	94.359	92.335
Straight_Hair	85.458	75.652	62.524	66.501	58.996
Wavy_Hair	86.772	85.850	77.797	72.607	83.785
Wearing_Earrings	92.203	85.752	78.655	82.295	75.323
Wearing_Hat	99.099	95.382	90.554	89.843	91.277
Wearing_Lipstick	92.676	93.035	92.147	88.292	96.354
Wearing_Necklace	89.480	63.894	40.894	63.421	30.175
Wearing_Necktie	96.703	85.544	76.156	80.215	72.488
Young	88.473	81.470	92.533	89.595	95.672
Cumulative avg	92.127	87.838	81.865	83.678	80.130
Attr avg mean	92.127	83.264	74.252	77.497	72.121

Table 10. Performance of VGG16 attribute classifier on CelebA (test set).

While EPR offers a unified way to quantify the balance between editing strength and unintended attribute changes, its reliance on explicit attribute labels is a fundamental limitation. In label-scarce or open-domain scenarios, such as LSUN-Church and AFHQ-Dog, EPR cannot be meaning-

fully computed. These results highlight both the usefulness and the scope constraints of label-based metrics, and motivate future work toward developing label-free editing precision metrics that remain valid across heterogeneous visual domains.

Model	Concept	recon.	Boundary [30]	Asymp [19]	Slider [7]	MasaCtrl [3]	SwiftEdit [21]	CASL-Steer
ResNet18	Smiling	0.679 \pm 0.289	1.231 \pm 0.976	3.199 \pm 2.182	0.949 \pm 0.479	1.685 \pm 1.375	3.359 \pm 2.064	4.465 \pm 2.319
	Big Nose	0.207 \pm 0.280	0.882 \pm 0.539	0.938 \pm 0.608	1.035 \pm 0.775	0.793 \pm 0.600	0.867 \pm 0.627	1.060 \pm 0.608
	Young	0.773 \pm 0.619	1.411 \pm 0.909	1.685 \pm 1.220	0.937 \pm 0.770	1.427 \pm 0.709	1.536 \pm 0.989	1.817 \pm 1.117
	Beards	0.763 \pm 0.669	1.165 \pm 0.974	1.739 \pm 1.268	0.919 \pm 0.383	2.059 \pm 1.541	1.255 \pm 0.884	2.161 \pm 1.080
	Blond Hair	0.110 \pm 0.032	0.876 \pm 0.794	1.173 \pm 1.002	0.760 \pm 0.548	1.173 \pm 0.678	1.302 \pm 1.014	1.386 \pm 1.213
MobileNetV2	Smiling	0.848 \pm 0.375	1.292 \pm 1.029	3.490 \pm 3.346	1.326 \pm 0.965	1.668 \pm 1.312	4.516 \pm 1.814	3.237 \pm 1.803
	Big Nose	0.169 \pm 0.081	0.995 \pm 0.423	0.872 \pm 0.292	1.381 \pm 0.820	0.759 \pm 0.555	1.045 \pm 0.749	1.261 \pm 0.650
	Young	0.799 \pm 0.571	1.532 \pm 1.099	1.808 \pm 1.757	1.070 \pm 0.540	1.407 \pm 0.379	1.797 \pm 1.058	1.799 \pm 1.256
	Beards	0.375 \pm 0.332	1.175 \pm 0.626	1.735 \pm 1.448	1.108 \pm 0.477	1.837 \pm 0.897	2.167 \pm 2.019	1.952 \pm 1.521
	Blond Hair	0.457 \pm 0.338	1.010 \pm 0.502	1.324 \pm 1.022	0.736 \pm 0.236	0.916 \pm 0.545	1.524 \pm 1.113	1.528 \pm 1.168
VGG16	Smiling	0.891 \pm 0.615	1.454 \pm 1.276	3.742 \pm 2.238	1.240 \pm 0.851	1.459 \pm 1.165	4.684 \pm 2.039	3.628 \pm 2.069
	Big Nose	0.907 \pm 0.248	0.669 \pm 0.609	0.734 \pm 0.464	0.896 \pm 0.721	0.766 \pm 0.528	0.855 \pm 0.583	0.902 \pm 0.482
	Young	0.830 \pm 0.747	1.493 \pm 0.856	1.718 \pm 0.991	1.003 \pm 0.760	1.396 \pm 0.721	1.634 \pm 0.916	1.653 \pm 1.067
	Beards	0.873 \pm 0.563	1.193 \pm 0.703	1.729 \pm 1.301	1.234 \pm 0.787	2.095 \pm 0.831	2.222 \pm 1.809	2.101 \pm 1.263
	Blond Hair	0.251 \pm 0.606	0.923 \pm 0.621	1.132 \pm 0.803	0.619 \pm 0.399	0.920 \pm 0.681	1.092 \pm 0.834	1.461 \pm 1.245
ViT-B/16	Smiling	1.144 \pm 0.848	1.301 \pm 0.894	2.366 \pm 1.388	1.640 \pm 1.161	1.404 \pm 0.976	2.426 \pm 1.402	2.371 \pm 1.375
	Big Nose	0.577 \pm 0.419	1.216 \pm 1.093	1.071 \pm 0.704	1.270 \pm 0.796	1.279 \pm 0.943	0.986 \pm 0.693	1.573 \pm 1.039
	Young	0.236 \pm 0.135	1.158 \pm 0.841	1.242 \pm 0.735	1.331 \pm 1.181	1.259 \pm 0.974	1.215 \pm 0.939	1.196 \pm 0.997
	Beards	0.248 \pm 0.189	1.351 \pm 1.199	1.383 \pm 0.702	1.171 \pm 0.806	1.589 \pm 1.083	1.548 \pm 0.999	1.176 \pm 1.016
	Blond Hair	0.763 \pm 0.113	0.943 \pm 0.709	1.138 \pm 0.905	0.753 \pm 0.511	1.069 \pm 1.031	0.908 \pm 0.680	1.061 \pm 0.717

Table 11. Editing Precision Ratio (EPR) scores for different methods and attribute-classifier combinations.

Concept	Metric	Recon.	Editing Methods					Explainable CASL-Steer
			Boundary	Asymp	Slider	MasaCtrl	SwiftEdit	
Gothic	CLIP-Score (\uparrow)	0.103 \pm 0.014	0.129 \pm 0.021	0.158 \pm 0.118	0.167 \pm 0.014	0.193 \pm 0.039	0.184 \pm 0.091	0.172 \pm 0.031
	LPIPS (\downarrow)	0.184 \pm 0.028	0.268 \pm 0.052	0.302 \pm 0.143	0.256 \pm 0.035	0.332 \pm 0.071	0.315 \pm 0.152	0.247 \pm 0.040
Red Brick	CLIP-Score (\uparrow)	0.118 \pm 0.016	0.145 \pm 0.024	0.174 \pm 0.132	0.183 \pm 0.016	0.196 \pm 0.042	0.211 \pm 0.097	0.203 \pm 0.037
	LPIPS (\downarrow)	0.198 \pm 0.030	0.279 \pm 0.060	0.310 \pm 0.149	0.276 \pm 0.038	0.338 \pm 0.078	0.327 \pm 0.162	0.251 \pm 0.044
Snowy	CLIP-Score (\uparrow)	0.132 \pm 0.019	0.154 \pm 0.027	0.182 \pm 0.146	0.189 \pm 0.018	0.219 \pm 0.049	0.226 \pm 0.124	0.209 \pm 0.034
	LPIPS (\downarrow)	0.213 \pm 0.033	0.291 \pm 0.067	0.326 \pm 0.164	0.284 \pm 0.041	0.353 \pm 0.083	0.341 \pm 0.174	0.258 \pm 0.048
Wooden	CLIP-Score (\uparrow)	0.111 \pm 0.015	0.139 \pm 0.023	0.164 \pm 0.128	0.174 \pm 0.017	0.204 \pm 0.047	0.198 \pm 0.102	0.218 \pm 0.052
	LPIPS (\downarrow)	0.191 \pm 0.031	0.273 \pm 0.058	0.298 \pm 0.156	0.268 \pm 0.036	0.329 \pm 0.080	0.316 \pm 0.170	0.244 \pm 0.043

Table 12. Evaluation on LSUN-Church dataset.

11. Full Hyperparameter Analysis Results

Due to space limitations in the main text, we provide the complete results of our hyperparameter analysis in the supplementary material.

11.1. Visualization Results

Visualization results for the main editing tasks and qualitative comparisons can be found in Human_Evaluation.pdf included in the supplementary material.

Concept	Metric	Recon.	Editing Methods					Explainable CASL-Steer
			Boundary	Asyryp	Slider	MasaCtrl	SwiftEdit	
Angry	CLIP-Score (\uparrow)	0.115 ± 0.017	0.142 ± 0.024	0.171 ± 0.148	0.182 ± 0.016	0.201 ± 0.045	0.219 ± 0.134	0.197 ± 0.039
	LPIPS (\downarrow)	0.204 ± 0.031	0.284 ± 0.062	0.318 ± 0.173	0.276 ± 0.039	0.347 ± 0.087	0.333 ± 0.182	0.253 ± 0.046
Sleepy	CLIP-Score (\uparrow)	0.108 ± 0.015	0.131 ± 0.020	0.159 ± 0.136	0.167 ± 0.014	0.185 ± 0.041	0.193 ± 0.121	0.176 ± 0.033
	LPIPS (\downarrow)	0.196 ± 0.030	0.273 ± 0.057	0.301 ± 0.159	0.268 ± 0.036	0.329 ± 0.082	0.317 ± 0.168	0.243 ± 0.045
Smiling	CLIP-Score (\uparrow)	0.121 ± 0.018	0.148 ± 0.025	0.179 ± 0.155	0.188 ± 0.017	0.208 ± 0.047	0.217 ± 0.145	0.204 ± 0.041
	LPIPS (\downarrow)	0.207 ± 0.033	0.289 ± 0.064	0.324 ± 0.166	0.277 ± 0.040	0.346 ± 0.089	0.335 ± 0.178	0.257 ± 0.048
Puppy-like	CLIP-Score (\uparrow)	0.134 ± 0.019	0.156 ± 0.027	0.188 ± 0.162	0.197 ± 0.018	0.221 ± 0.052	0.226 ± 0.152	0.233 ± 0.056
	LPIPS (\downarrow)	0.215 ± 0.034	0.296 ± 0.069	0.332 ± 0.178	0.283 ± 0.041	0.359 ± 0.093	0.341 ± 0.185	0.249 ± 0.050

Table 13. Evaluation on the AFHQ-Dog dataset.

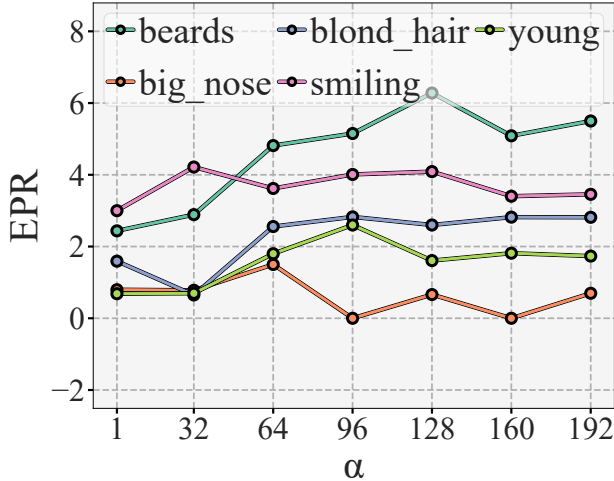


Figure 5. EPR vs. α for top- k = 1 (all concepts).

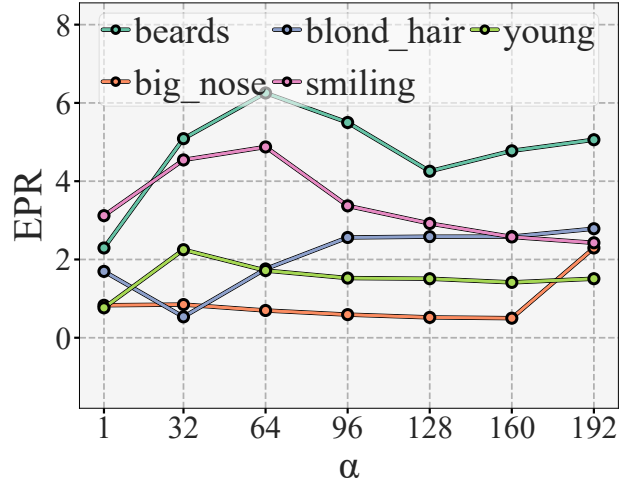


Figure 7. EPR vs. α for top- k = 4 (all concepts).

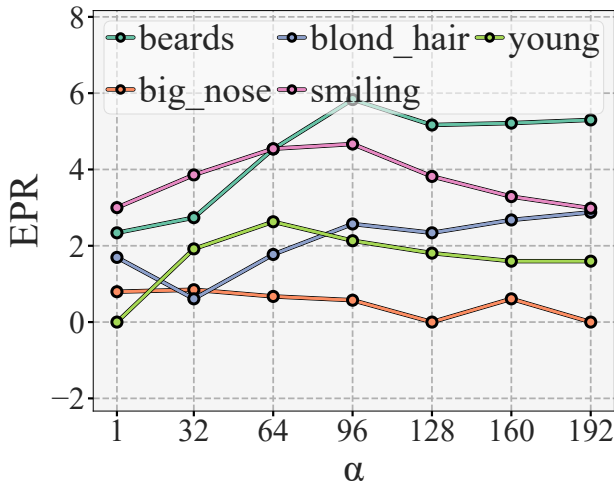


Figure 6. EPR vs. α for top- k = 2 (all concepts).

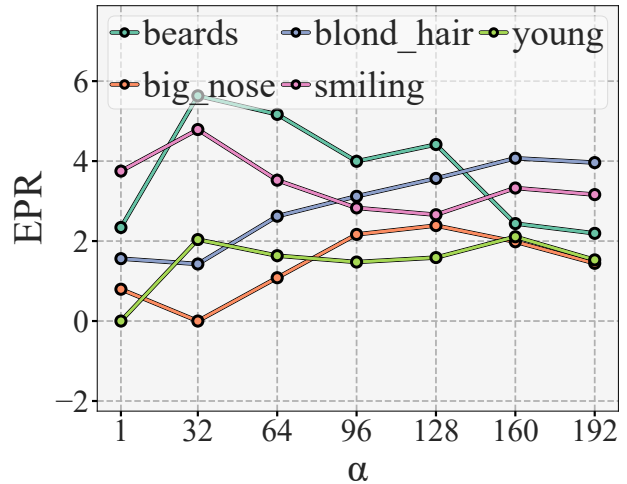


Figure 8. EPR vs. α for top- k = 8 (all concepts).

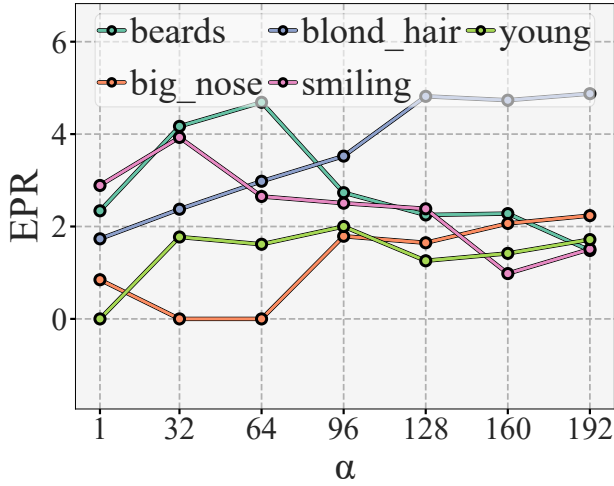


Figure 9. EPR vs. α for top- k = 16 (all concepts).

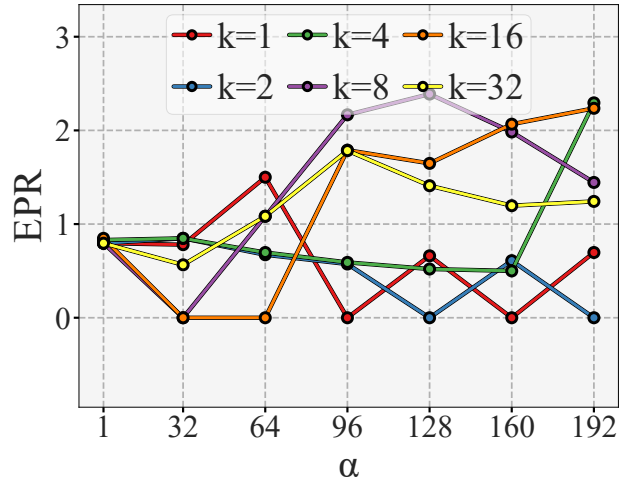


Figure 12. EPR vs. α for Big Nose.

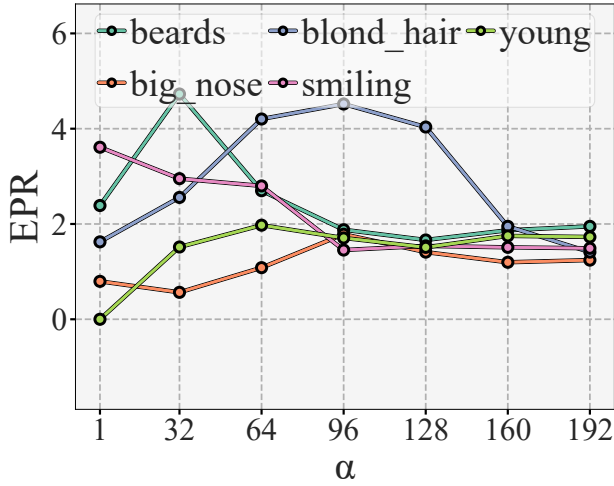


Figure 10. EPR vs. α for top- k = 32 (all concepts).

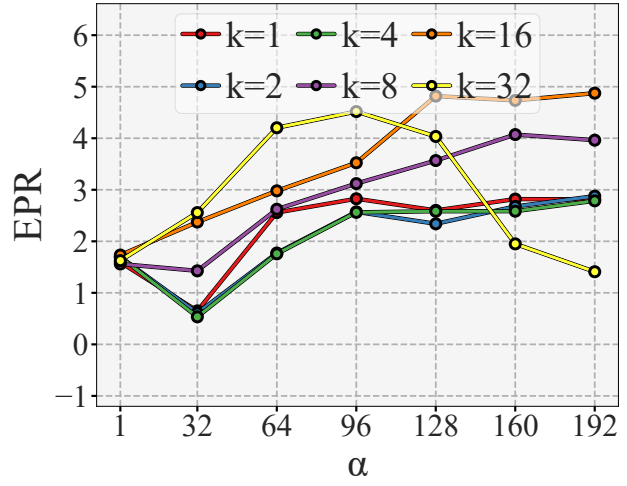


Figure 13. EPR vs. α for Blond Hair.

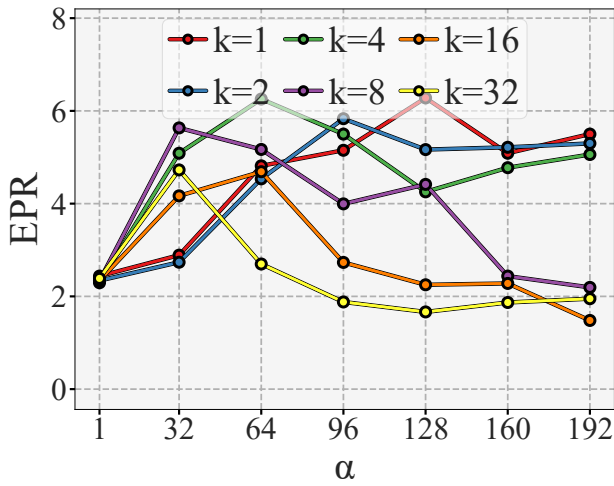


Figure 11. EPR vs. α for Beards.

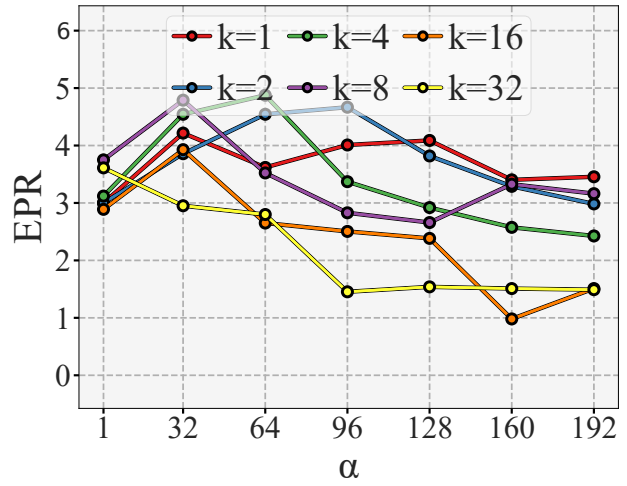


Figure 14. EPR vs. α for Smiling.

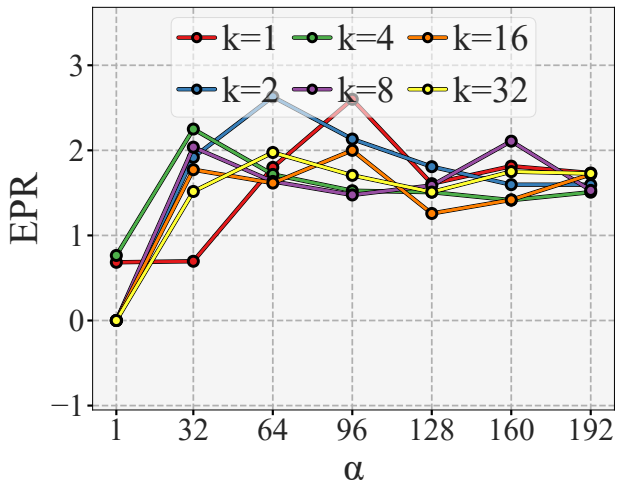


Figure 15. EPR vs. α for Young.

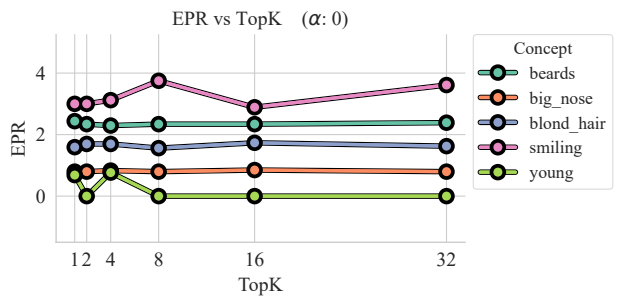


Figure 16. EPR vs. top- k for $\alpha = 0$.

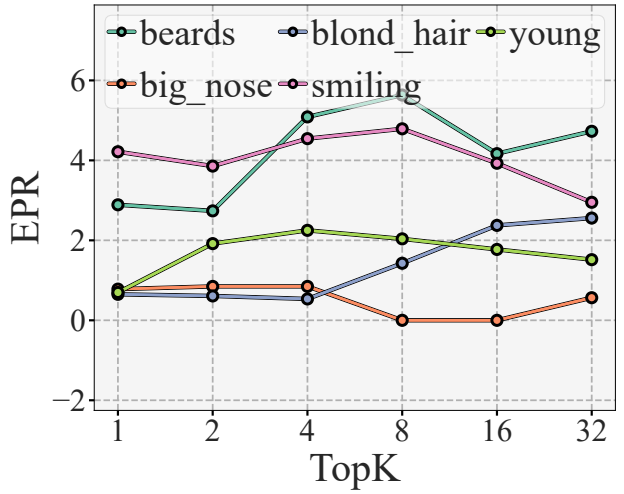


Figure 18. EPR vs. top- k for $\alpha = 32$.

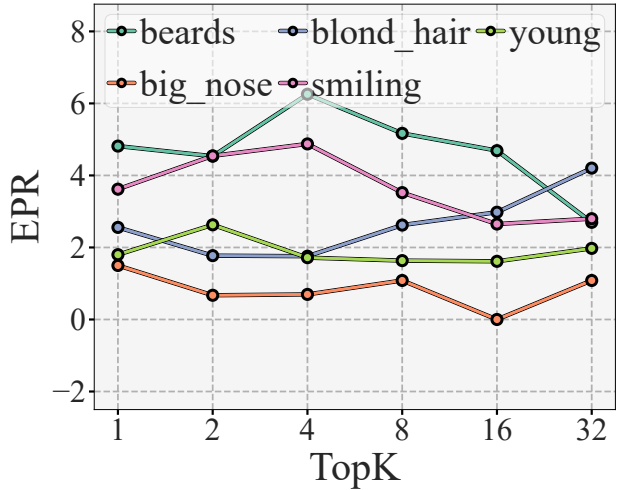


Figure 19. EPR vs. top- k for $\alpha = 64$.

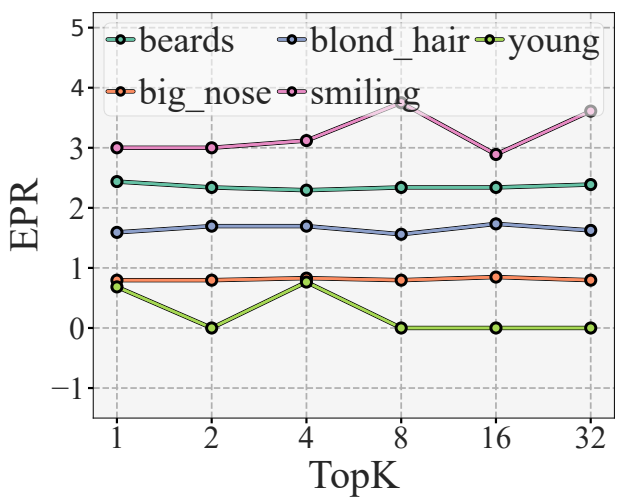


Figure 17. EPR vs. top- k for $\alpha = 1$.

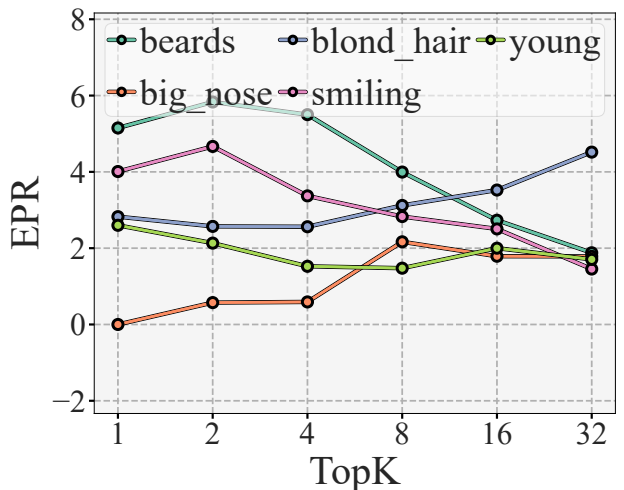


Figure 20. EPR vs. top- k for $\alpha = 96$.

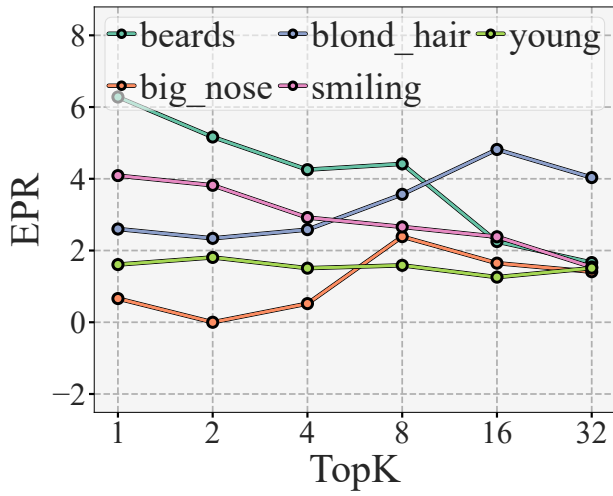


Figure 21. EPR vs. top- k for $\alpha = 128$.

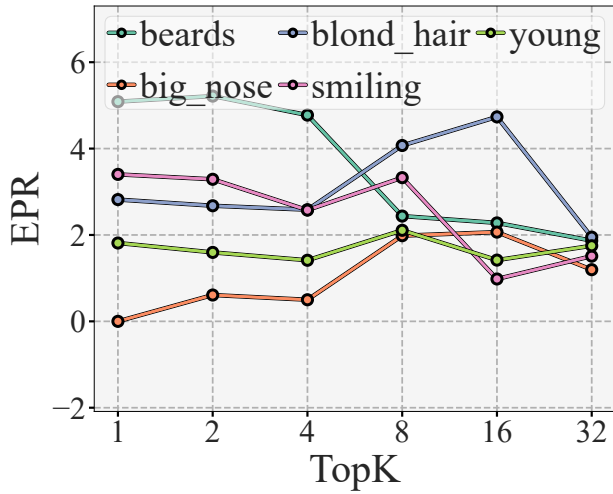


Figure 22. EPR vs. top- k for $\alpha = 160$.

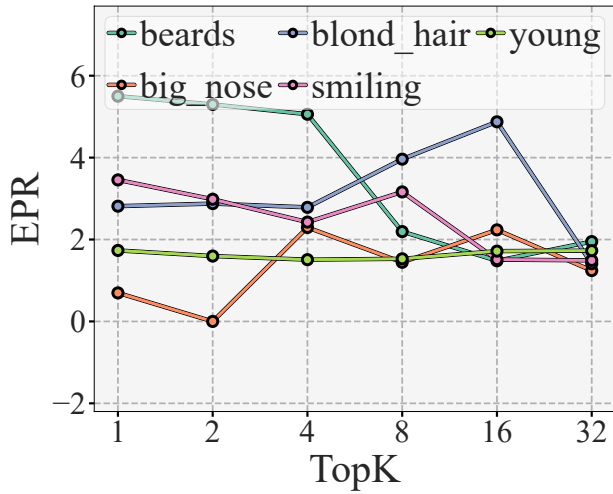


Figure 23. EPR vs. top- k for $\alpha = 192$.